Earth Planet. Sci. Lett. 627 (2024) 118566

Contents lists available at ScienceDirect

Earth and Planetary Science Letters

journal homepage: www.elsevier.com/locate/epsl

Shallow carbonate geochemistry in the Bahamas since the last interglacial period

Stacey Edmonsond[a,b,*], Matthew D. Nadeau[a], Andrew C. Turner[d], Ziman Wu[d], Emily C. Geyman[a,e], Anne-Sofie C. Ahm[a,b], Blake Dyer[b], Sergey Oleynik[a], David McGee[c], Daniel A. Stolper[d], John A. Higgins[a], Adam C. Maloof[a]

[a] Department of Geosciences, Princeton University, Princeton, NJ, USA
[b] School of Earth and Ocean Sciences, University of Victoria, Victoria, BC, Canada
[c] Department of Earth, Atmospheric and Planetary Sciences, Massachusetts Institute of Technology, Cambridge, MA, USA
[d] Department of Earth and Planetary Science, University of California, Berkeley, CA, USA
[e] Division of Geological and Planetary Sciences, California Institute of Technology, Pasadena, CA, USA

ARTICLE INFO

Editor: A. Jacobson

GitHub repository: Data and code for 'Shallow carbonate geochemistry in the Bahamas since the last interglacial period' (Edmonsond et al.) (Original Data)

Keywords:
last interglacial period
Bahamas
carbonates
carbon isotopes
oxygen isotopes
stratigraphy

ABSTRACT

The carbon isotope composition (δ^{13}C) of ancient shallow-water carbonates frequently is used to reconstruct changes to Earth's global carbon cycle and to perform chemostratigraphic correlation. However, previous work demonstrates that local banktop processes also exert an important control on shallow carbonate δ^{13}C as well as other isotope systems like δ^{18}O. To effectively interpret ancient δ^{13}C records, we must understand how both global carbon cycle perturbations and changes to local conditions are translated to the stratigraphic record. Modern environments, while imperfect analogues, can serve as a guide for interpreting physical and geochemical records of more ancient environments. Shallow carbonate strata from the most recent Pleistocene glacial cycles, which drove high-amplitude perturbations to sea level, temperature, and pCO$_2$ without significantly altering the δ^{13}C of global-mean seawater DIC, present an opportunity to begin untangling signals of global and local processes. However, the geochemistry of Pleistocene platform carbonates largely was overprinted by dissolution and meteoric diagenesis during glacial sea level lowstands. To understand how shallow carbonate geochemistry has changed during the Pleistocene, we instead look to the periplatformal slope and proximal basins. These deep environments serve as a refuge for carbonate produced on the shelf and exported to the slope, and contain a record of shallow carbonate geochemistry that persists across glacial cycles. We study 21 short piston cores from around Bahamian platforms to quantify differences in banktop production and geochemistry between the Holocene interglacial, the last glacial period, and the last interglacial (LIG) period. We show that mud production persists on the periplatformal slopes during the last glacial period, but differences in geochemistry between glacial and interglacial carbonates are a complex function of surface conditions and diagenesis. In contrast, Holocene and LIG carbonates show no evidence of post-depositional alteration, and offer the chance to study differences in δ^{13}C and δ^{18}O between interglacials. We find that while the δ^{13}C of aragonite mud is the same during the Holocene and LIG, the LIG carbonate factory may have delivered more aragonite mud to the periplatform. In addition, the mean δ^{18}O of this mud is elevated compared to the Holocene. We posit that these differences are caused by changes to regional climate and LIG surface conditions.

1. Introduction

The δ^{13}C of shallow water carbonates (δ^{13}C$_{carb}$) frequently is used to reconstruct Earth's ancient carbon cycle (e.g., Kump and Arthur, 1999). However, recent studies have demonstrated that shallow δ^{13}C$_{carb}$ is not a simple recorder of the δ^{13}C of global open-ocean or even local-mean seawater dissolved inorganic carbon (δ^{13}C$_{DIC}$) (e.g., Swart and Eberli, 2005; Swart et al., 2009; Geyman and Maloof, 2019; Ahm et al., 2021). Instead, banktop processes like meteoric diagenesis (e.g., Allan and Matthews, 1982), marine diagenesis (e.g., Ahm et al.,

---

* Corresponding author at: School of Earth and Ocean Sciences, University of Victoria, Victoria, BC, Canada.
E-mail address: sedmonsond@uvic.ca (S. Edmonsond).

https://doi.org/10.1016/j.epsl.2023.118566
Received 19 May 2023; Received in revised form 27 November 2023; Accepted 29 December 2023

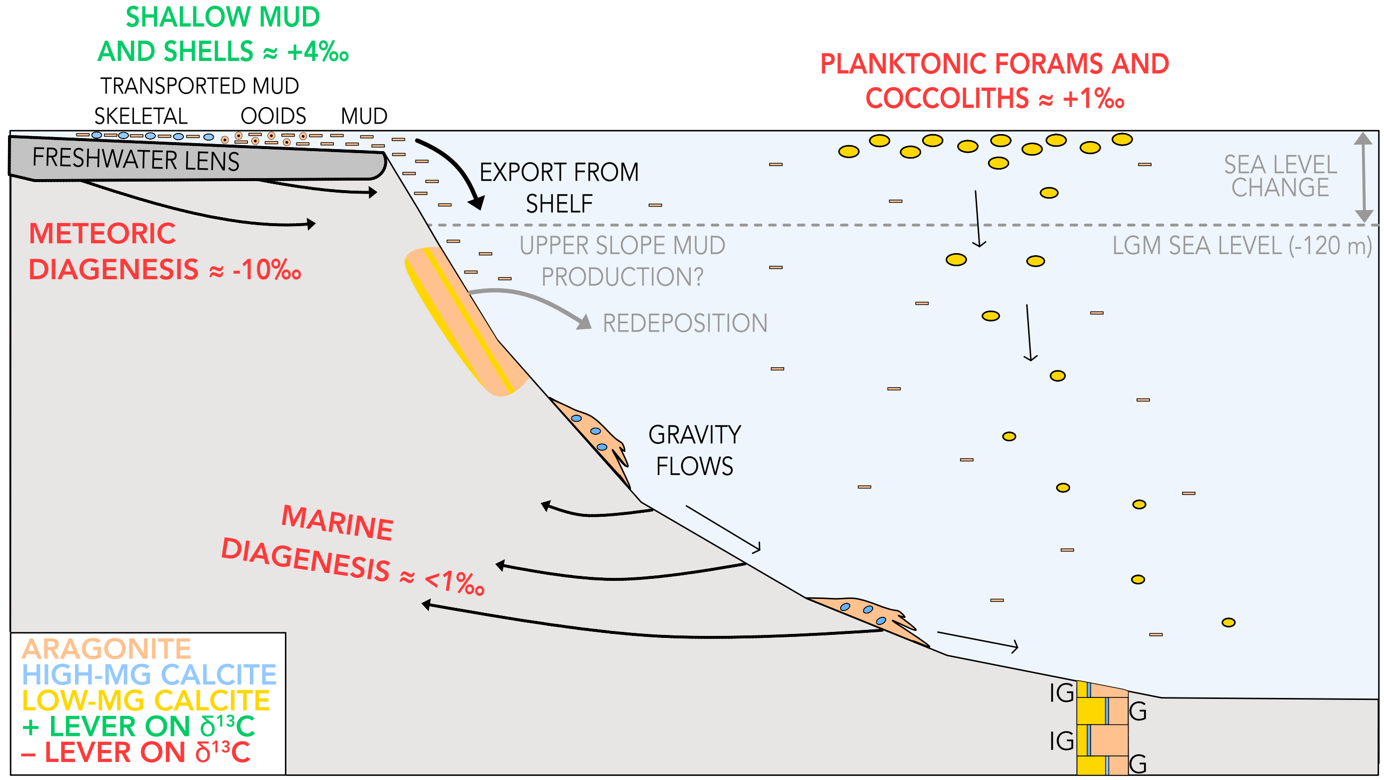

Fig. 1. On the shallow banktop, photosynthesis elevates $\delta^{13}C_{carb}$ above the expected value for carbonate precipitated in equilibrium with open-ocean DIC (Geyman and Maloof, 2019). Bahamian banktop carbonate primarily is aragonite with some high-magnesium calcite (HMC) (Swart et al., 2009), while pelagic planktonic forams and coccoliths produced in the mixed layer of the open ocean are composed of low-magnesium calcite (LMC). Exported banktop carbonate raises both the $\delta^{13}C$ and aragonite fraction of slope carbonate compared to background pelagic sedimentation (Swart and Eberli, 2005). When sea level falls below the platform edge during glacial sea level lowstands, aragonite input is reduced and the fraction of pelagic LMC increases. More limited aragonite mud production likely persists on the upper slopes (Geyman et al., 2022), and older sediment also may be redeposited through winnowing or as gravity flows. While sea level is low, banktop carbonate on the subaerially exposed shelf is cemented and altered by meteoric waters while the periplatformal slope remains submerged. On longer timescales, metastable aragonite and HMC recrystallize to LMC during early marine diagenesis at the seafloor (Higgins et al., 2018).

2018; Higgins et al., 2018), and local carbon cycling (e.g., Geyman and Maloof, 2019, 2021) decouple $\delta^{13}C_{carb}$ from open-ocean $\delta^{13}C_{DIC}$ and generate intrashelf $\delta^{13}C_{carb}$ variability. Many of these local processes can change $\delta^{13}C_{carb}$ on timescales shorter than the 100 kyr oceanic residence time of DIC, complicating interpretations of global carbon cycle change (e.g., Schobben et al., 2017). By studying changes in shallow $\delta^{13}C_{carb}$ that occur on <100 kyr timescales, we can isolate the local drivers of meter-scale $\delta^{13}C_{carb}$ variability from steady-state changes in global $\delta^{13}C_{DIC}$. Attendant changes in other geochemical proxies that are sensitive to local environment, such as carbonate $\delta^{18}O$, also can be leveraged to constrain the relative importance of these processes. Characterizing the geochemical fingerprints of local processes can improve interpretations of longer-term swings in $\delta^{13}C_{carb}$ in the geologic record.

Shallow carbonates from the most recent Pleistocene glacial-interglacial cycles present an opportunity to study the sensitivity of $\delta^{13}C_{carb}$ to local environmental change. These well-constrained climate perturbations serve as controlled natural experiments where various local and global environmental parameters (i.e., sea level and temperature) are adjusted while global-mean seawater $\delta^{13}C_{DIC}$ remains nearly constant (e.g., Curry et al., 1988; Bengtson et al., 2021). Here, we primarily focus on comparing $\delta^{13}C_{carb}$ between different interglacial periods rather than across glacial-interglacial transitions. However, we also consider key points of contrast between glacial and interglacial geochemistry.

Sea level highstands are represented by carbonate deposition on shallow platforms, while lowstands are expressed as physical and geochemical unconformities caused by erosion and meteoric diagenesis during subaerial exposure of the shelf (Allan and Matthews, 1982; Dyer et al., 2015). In other words, shallow platforms do not preserve synglacial carbonate because the banktop carbonate factory shuts down or migrates to the periplatformal slopes when sea level drops below the shelf edge, and production on the banktop only resumes when sea level rises again during the next interglacial. Therefore, meter-scale variability in shallow $\delta^{13}C_{carb}$ more likely is related to differences in local banktop conditions between different highstands (i.e., interglacial periods) than to the more drastic transitions between highstand and lowstand conditions (i.e., glacial-interglacial cycles). The last interglacial period (LIG, ∼130−115 ka), for instance, was marked by higher sea level (1.2–5.3 m above modern; Dyer et al., 2021) and higher global-mean sea surface temperatures (0.2–0.8 °C above pre-industrial; Hoffman et al., 2017), but the estimated difference in global-mean $\delta^{13}C_{DIC}$ compared to the Holocene is only ∼0.2‰ (Bengtson et al., 2021).

We focus here on the Bahamian archipelago, which is located in the western Atlantic Ocean along the southernmost continental margin of North America. The Bahamas are a subsiding carbonate depositional system that has accumulated at least 7 km of carbonate rock since the Jurassic (Mullins and Lynts, 1977). In theory, the uppermost portion of this shallow-water platform carbonate stratigraphy is an ideal target for constraining changes in the value and variability of shallow $\delta^{13}C_{carb}$ between the LIG and the Holocene. Unfortunately, the geochemistry of sediments older than 3–5 kyr was overprinted by karst and meteoric diagenesis during the last glacial period (Swart and Eberli, 2005). However, a significant fraction of carbonate produced on the banktop is exported to the periplatformal slope and proximal basins (e.g., Milliman et al., 1993; Schlager et al., 1994), where it mixes with pelagic carbonate (Swart and Eberli, 2005) and then undergoes early marine diagenesis at the seafloor (Ahm et al., 2018; Higgins et al., 2018) (Fig. 1). Periplatform sediments are protected from meteoric diagenesis during

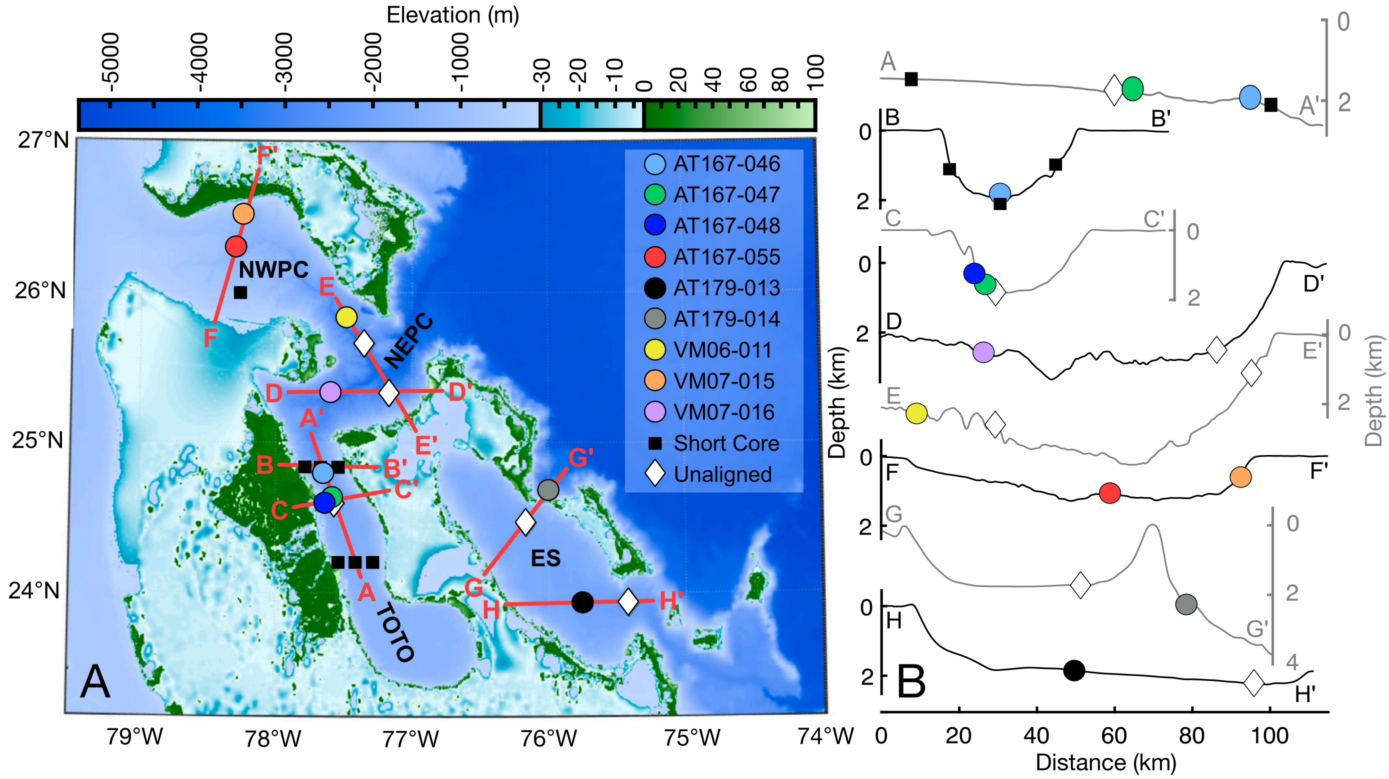

Fig. 2. A) Periplatformal slope and proximal basin cores come from the Tongue of the Ocean (TOTO), Northeast Providence Channel (NEPC), Northwest Providence Channel (NWPC), and Exuma Sound (ES). Elevation data are from the GEBCO_2020 Grid with 15 arc-second resolution (https://www.gebco.net/). B) Bathymetry profiles along the transects labeled in A.

lowstands, and thus contain a record of banktop $\delta^{13}C_{carb}$ that is better preserved across glaciations.

Here, we present new stratigraphic records for 21 Pleistocene-Holocene sediment cores from 790 to 2,700-meter-deep waters around Bahamian carbonate platforms (Fig. 2). We leverage combined $\delta^{13}C_{carb}$, $\delta^{18}O_{carb}$, $\delta^{44/40}$Ca, mineralogy, trace element, Δ_{47}, and sedimentation rate measurements to deconvolve signals for shallow export, pelagic sedimentation, and early marine diagenesis in these cores during the Holocene and LIG.

1.1. Origins of carbon isotopic variability in shallow carbonates

Previous workers have used modern environments as natural laboratories to characterize $\delta^{13}C_{carb}$ variability – not through time, but rather in space (e.g., Gischler et al., 2009; Swart et al., 2009; Geyman and Maloof, 2019, 2021). Geyman and Maloof (2019) showed that because banktop $\delta^{13}C_{DIC}$ is elevated during daily peak carbonate production, banktop $\delta^{13}C_{carb}$ is higher than the expected value for carbonate precipitated in equilibrium with local-mean DIC. As a result, export of high-δ^{13}C sediment from the shelf raises the δ^{13}C of periplatform carbonate relative to pelagic and benthic sources, compounding the mineralogical effect identified by Swart and Eberli (2005) (Fig. 1). The primary δ^{13}C and mineralogy of periplatform carbonate, therefore, partially depend on the relative input of different carbonate sources (Fig. 3; Swart and Eberli, 2005; Swart, 2008).

On the banktop, Geyman and Maloof (2021) showed that different carbonate grain types have distinct isotopic signatures, with δ^{13}C values spanning a range of ∼10‰ in their study area on the modern Great Bahama Bank. Consequently, the average δ^{13}C of a given rock could be partly controlled by the type, abundance, and size distribution of its constituent grains (i.e., its sedimentary facies). This observation is important because stratigraphic sections through shallow carbonates commonly are composed of meter-scale upward-shallowing parasequences – particular facies stacking patterns related to filling of accommodation space. Numerical experiments using data from the modern Great Bahama Bank show that localized facies changes can drive 1−3‰ shifts in $\delta^{13}C_{carb}$ on the scale of a single parasequence (Geyman and Maloof, 2021). However, these experiments could not account for the possibility that temporal changes to local surface conditions could also shift the average, or bulk, δ^{13}C of banktop carbonate within or between parasequences. Even if global-mean $\delta^{13}C_{DIC}$ remains constant, perturbations to sea level and climate could change bulk $\delta^{13}C_{carb}$ locally by altering variables like banktop restriction and the large-scale distribution of facies belts (Gischler et al., 2009; Geyman and Maloof, 2021), diurnal cycling of photosynthesis and respiration (Geyman and Maloof, 2019), nutrient delivery (Swart et al., 2014), input of terrestrially-derived remineralized organic carbon (Patterson and Walter, 1994), local microbial activity (Andres et al., 2006; Ingalls et al., 2020), and carbon isotope fractionation between DIC and organic matter (Burkhardt et al., 1999).

The δ^{13}C of carbonate mud is nearly homogeneous across the Great Bahama Bank because the fine fraction of banktop sediment is easily transported (and therefore well-mixed; Fig. 3A), and precipitation of mud in the water column peaks in unrestricted bank-margin waters (Broecker and Takahashi, 1966; Geyman et al., 2022). The δ^{13}C of mud thus serves as a measure of banktop $\delta^{13}C_{carb}$ that is less sensitive to cross-shelf geochemical gradients and facies variability – meaning that by comparing the δ^{13}C of LIG and Holocene banktop mud, we can determine whether differences in LIG surface conditions altered local-mean $\delta^{13}C_{carb}$, or if parasequence-scale $\delta^{13}C_{carb}$ fluctuations more likely are caused by facies changes. Here we ask the question, has the average δ^{13}C of banktop mud exported to the periplatform changed in response to different global and local environmental forcings between the Holocene and LIG?

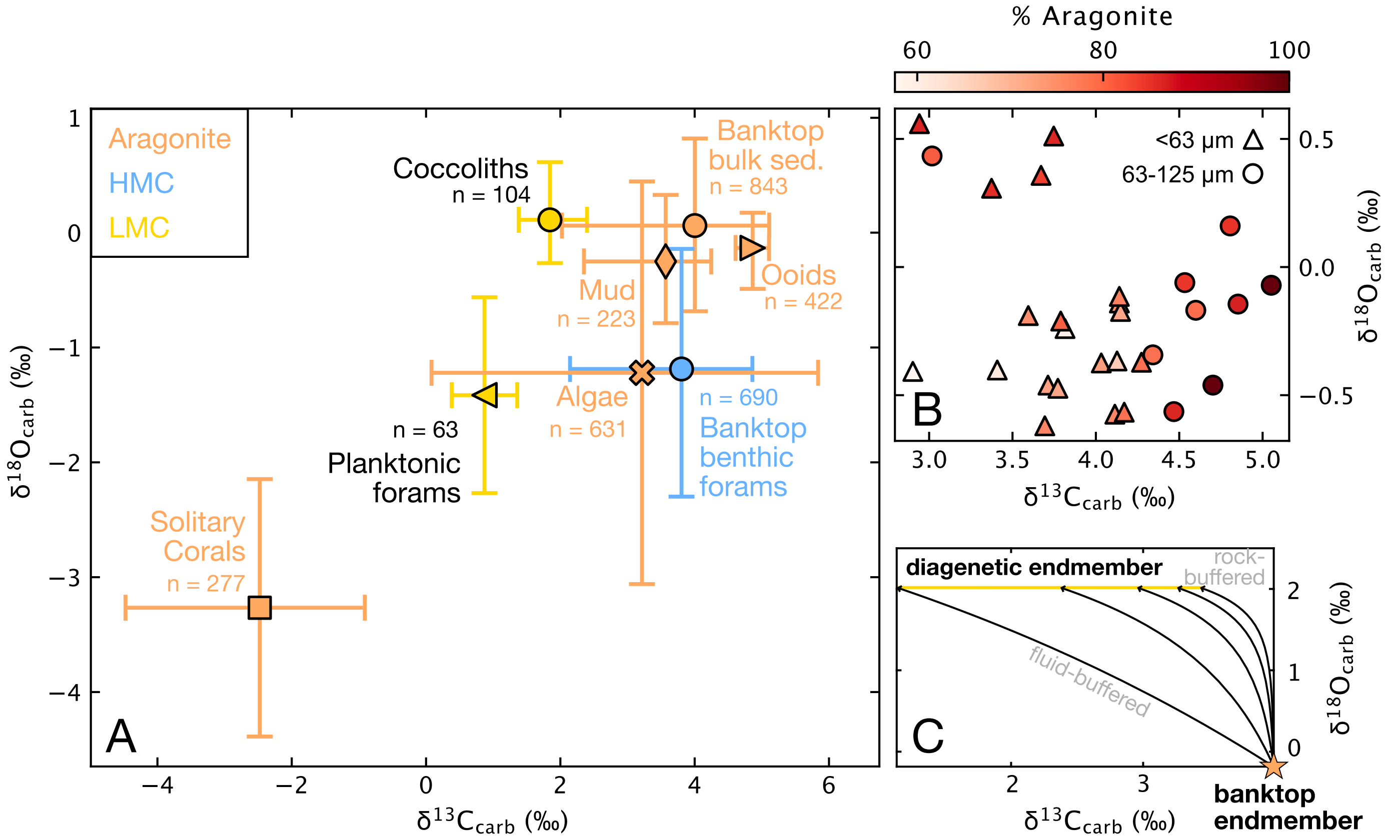

Fig. 3. A) Mean δ^{13}C and δ^{18}O for banktop and pelagic endmembers plotted with 5th and 95th percentiles. Banktop data are from Geyman and Maloof (2021), with additional bulk sediment data from Swart et al. (2009) ($n = 272$) and algae data from Lowenstam and Epstein (1957) ($n = 23$). Endmembers are color-coded by primary mineralogy, but note that banktop bulk sediment and mud also contain variable amounts of HMC. Banktop forams are *Peneroplis proteus*. Planktonic foram and coccolith data are from Pleistocene-Holocene deep-water cores around the Bahamas and the Caribbean Sea (Table S7); δ^{18}O data included here are from the Holocene and LIG. B) To approximate the mineralogy and δ^{13}C of the exported banktop carbonate endmember, we consider 29 mud (<63 μm) and fine (63–125 μm) sediment size fraction samples from near the shelf edge with XRD mineralogy measurements. The mean aragonite content of this population is $78 \pm 10\%$ ($\mu \pm 1\sigma$), while δ^{13}C is 3.99 ± 0.58‰ and δ^{18}O is -0.18 ± 0.33‰. C) Recrystallization in deep, cold bottom waters increases $\delta^{18}O_{carb}$ and decreases $\delta^{13}C_{carb}$. We simulate potential alteration paths for the banktop endmember defined by the samples in B during early marine diagenesis at 4.5 °C (the average bottom water temperature at our core sites) in interglacial seawater (Table S6; Ahm et al., 2018). Here, we plot alteration trajectories for a range of fluid- to rock-buffered conditions. Fig. S19 shows alteration paths under the full range of bottom water temperatures for our cores (3.1 to 9.3 °C).

2. Methods

2.1. Sample collection and preparation

We obtained samples from piston cores curated by the Lamont-Doherty Core Repository of the Lamont-Doherty Earth Observatory. Dry cores were collected between 1952 and 1959 by the Atlantis (AT167 and AT179) and VEMA (VM06, VM07, and VM15) expeditions and stored at room temperature. Wet cores were collected during Knorr expeditions in 1998 (NV923) and stored in D-tubes at 4.5 °C. Samples were collected at 5 cm intervals following the methodology detailed in the supplementary material. All geochemical measurements are made on aliquots of powders homogenized using a drill or mortar and pestle.

2.2. Thin section petrography

We prepared thin sections of 88 samples from 9 different cores. We obtained point counts ($n \geq 300$) of Holocene ($n = 11$), last glacial period ($n = 26$), LIG ($n = 20$), and pre-LIG ($n = 17$) thin sections to estimate the abundance of all major allochems (mud, planktonic and benthic foraminifera, skeletal fragments, gastropods, bivalves, ostracods) and various rare allochems.

2.3. Mineralogy

We collected powder X-ray diffraction (XRD) patterns for 409 periplatform samples, 29 banktop samples, standards for aragonite (Morocco aragonite), HMC (sand dollars), and LMC (Iceland spar), and 42 calibration mixtures (known mixtures of the endmember standards) using a Bruker D8 Discover X-Ray Diffractometer in the Imaging and Analysis Center at Princeton University. We estimate phase contributions by treating each sample as a linear combination of carbonate endmembers following the procedure detailed in the supplementary material. For 42 calibration mixtures and 7 replicate analyses, mean absolute error is 3.85% for aragonite ($n = 28$), 4.45% for HMC ($n = 46$), and 4.97% for LMC ($n = 41$) (Fig. S2).

2.4. Carbon and oxygen isotope measurements

We measured carbonate δ^{13}C and δ^{18}O on all samples ($n = 1{,}601$) using a Sercon continuous flow isotope ratio mass spectrometer (CF-IRMS) at Princeton University following the procedure outlined in the supplementary material. We report δ^{13}C and δ^{18}O relative to Vienna Pee Dee Belemnite (VPDB). Mean precision is < 0.1‰ (1σ) for δ^{13}C and < 0.25‰ (1σ) for δ^{18}O.

2.5. Major and trace element analyses

Following the procedure outlined in the supplementary material, we measured major and trace element concentrations from aliquots of dissolved powders for 233 samples from 12 different cores using a Thermo-Fisher I-Cap Q inductively-coupled plasma mass spectrometer (ICP-MS) at Princeton University. Metal to Ca ratios of samples were determined using a set of matrix-matched in-house calibration standards which spanned the sample range. Reported ratios are an average of at least 2 measurements. The external reproducibility of these measurements is estimated at <5% (2σ) based on replicate measurements of NIST SRM 88b, a dolomitic limestone.

2.6. Ca isotope measurements

We made calcium isotope measurements on a subset ($n = 45$) of dissolved samples using a Thermo-Fisher Scientific Neptune Plus multi-collector inductively-coupled plasma mass spectrometer (MC-ICP-MS) at Princeton University following the procedure detailed in the supplementary material. Carbonate $\delta^{44/40}$Ca values are reported relative to modern seawater, with $\delta^{44/40}\text{Ca}_{\text{seawater}}$ defined as 0‰. Long-term external reproducibility is estimated by repeat measurements of Ca isotope standards which have been taken through the full chemical procedure (column chromatography and mass spectrometry) with each batch of samples. We report external reproducibility using the measured value of SRM 915b relative to modern seawater (-1.19 ± 0.17‰ 2σ; $n = 47$), which is indistinguishable from previously reported values. Additional measurements of NIST SRM 88b, an in-house limestone, and modern seawater were used to monitor the accuracy of each run. Reproducibility (2 s.e.) of each sample is estimated by replicated measurements from different analytical sessions, and typically is better than 0.10‰.

2.7. Clumped-isotope measurements

Carbonate clumped-isotope (Δ_{47}) analyses were performed on 17 periplatform core samples in the Department of Earth and Planetary Science at the University of California, Berkeley. Methodologies follow those described in Hodgin et al. (2022) and Geyman et al. (2022) and are summarized in the supplementary material. Δ_{47} values constrain the relative abundance of carbonate groups with multiple rare isotopes (dominantly ^{13}C–^{18}O bonds) vs. that for a random distribution (Ghosh et al., 2006). Δ_{47} values are a monotonic function of temperature for samples that form in internal isotopic equilibrium (Ghosh et al., 2006). As such, Δ_{47} can be used to infer seawater temperature at the time of carbonate precipitation. We calculated Δ_{47}-based temperatures using the calibration given in Anderson et al. (2021). External precision of Δ_{47} was determined based on the pooled standard deviation of the samples and is ± 0.009 (1σ).

2.8. Radiocarbon dating

Radiocarbon ages for 32 samples from 9 different cores were measured at the National Ocean Sciences Accelerator Mass Spectrometry (NOSAMS) laboratory following the procedure outlined in the supplementary material. In all analyses, we report calibrated calendar ages (in years B.P.) with 1σ error.

2.9. U-Th dating

U-Th dating of 4 periplatform core samples was performed at MIT following the procedure outlined in the supplementary material. Two samples produced low $^{234}\text{U}/^{238}\text{U}$ values consistent with diagenetic U loss, and did not yield reliable ages. U-Th ages from cores AT167-047 (137.3 ± 9.7 ka) and AT167-048 (102.3 ± 5.6 ka) broadly support our identification of the LIG. Data and calculated ages are in Table S3.

2.10. Estimating mineralogical endmember $\delta^{13}C$

We leverage combined mineralogy and bulk sediment δ^{13}C measurements to infer the δ^{13}C of different mineralogical endmembers. We evaluate this relationship using Equation (1), where δ terms are the δ^{13}C of each mineralogical endmember (to be inferred from the data) and F terms are measured percentages of each mineralogical endmember.

$$\delta^{13}C_{bulk} = (F_{arag} \times \delta_{arag}) + (F_{HMC} \times \delta_{HMC}) + (F_{LMC} \times \delta_{LMC}) \quad (1)$$

Our inverse model accounts for measurement uncertainty in both mineralogy and bulk sediment δ^{13}C, and is built using the Python probabilistic programming package PyMC (Abril-Pla et al., 2023). The priors for endmember δ^{13}C are normal Gaussian distributions with $\mu = 2.7$ (aragonite) or $\mu = 1.0$ (HMC and LMC) and $\sigma = 3$. Posterior δ^{13}C distributions are sampled with the No U-Turn Sampler in PyMC.

2.11. Age models

We approach age model construction with the goal of confidently differentiating Holocene, last glacial, LIG, and pre-LIG core samples. More specifically, we aim to isolate the intervals of time when the shelf is flooded and the banktop carbonate factory is active. Due to high-frequency $\delta^{18}\text{O}_{\text{carb}}$ variability and limitations of radiometric methods, we do not attempt to refine sample age estimates within these intervals.

In each core with sufficient $\delta^{18}\text{O}_{\text{carb}}$ signal preservation ($n = 9$ cores), we identify tie points for the onset of the LIG, the termination of the LIG, and the onset of the current Holocene interglacial (Figs. 4C and S4). For our purposes, an interglacial is approximately bounded by the earliest coral reef growth after the banktop is flooded and the latest coral reef growth preceding subaerial exposure. We therefore use previously published ^{14}C and U-Th ages from corals (Holocene and LIG) and mangrove peats (Holocene) to assign liberal ages and uncertainties (2σ) to the LIG ($130.18 \pm 1.93 - 115.49 \pm 1.15$ ka) and Holocene ($7.85 \pm 2.39 - 0$ ka) boundaries (Figs. 4A and S3, Table S4). We then use a combination of ^{14}C ages, U-Th ages, and δ^{18}O to locate time-equivalent points for each boundary in the periplatform record. Detailed methodology for tie point identification is in section 1.9 of the supplementary material.

To account for uncertainty in tie point and ^{14}C ages, and to assign ages to intermediate samples, we implement a Bayesian Markov chain Monte Carlo (MCMC) model with a Gibbs sampler (Schoene et al., 2019). The MCMC model refines age estimates for each sample by considering uncertainty in the underlying and overlying ages while imposing stratigraphic superposition. In all subsequent analyses, we treat the MCMC output for each core as its best-fit age model (Fig. 4B). Although we cannot establish full age models for the shortest cores ($n = 7$), we assign constituent samples to the Holocene or last glacial period.

We acknowledge that there are many possible ways to define the Holocene and LIG boundaries in our cores, and that radiometric age constraints from corals may not precisely capture the absolute timing of banktop flooding. However, since our goal is to compare banktop carbonate geochemistry during different highstands, we consider that internal consistency is more important than the exact age and position of tie points. Absolute ages of the Holocene and LIG boundaries affect sedimentation rate estimates, but otherwise do not impact our results.

3. Results

3.1. $\delta^{18}O_{carb}$, $\delta^{13}C_{carb}$, trace element, and mineralogy stratigraphies

To identify broad trends in periplatform geochemistry during and since the LIG, we use our MCMC age models to construct $\delta^{18}\text{O}_{\text{carb}}$,

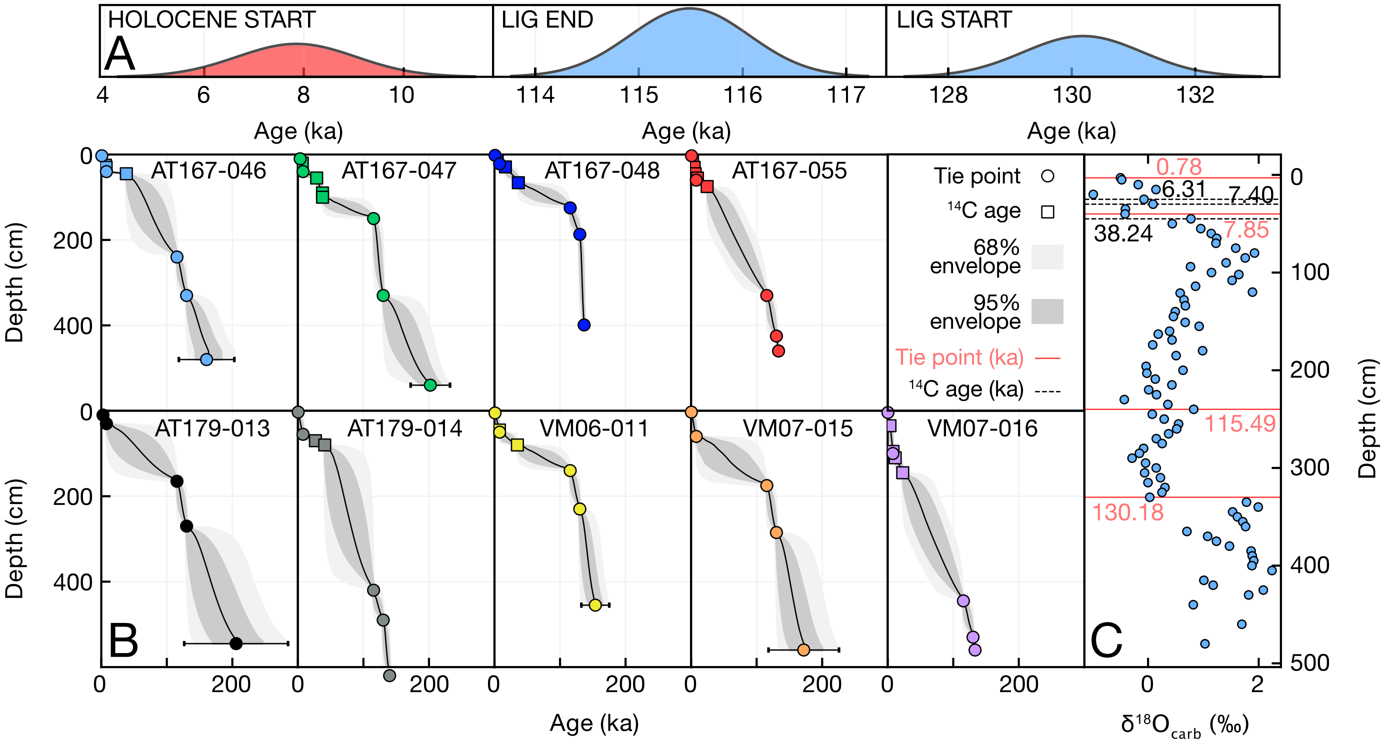

Fig. 4. A) Probability distributions for the timing of the Holocene and the LIG based on dated corals and mangrove peat horizons in the literature (see supplementary material, section 1.9). B) MCMC age-depth models for 9 aligned cores plotted with 68% and 95% confidence envelopes. Tie points and ^{14}C ages are plotted with 2σ uncertainty. C) Example tie point identification for core AT167-046.

$\delta^{13}C_{carb}$, Sr/Ca, and mineralogy stratigraphies for each core (Fig. 5). Downcore trends in both $\delta^{18}O_{carb}$ and $\delta^{13}C_{carb}$ generally are similar after alignment, but absolute $\delta^{18}O_{carb}$ and $\delta^{13}C_{carb}$ vary by ∼2‰ and ∼3‰, respectively, at a given time (Fig. 5A). Displacements between individual $\delta^{13}C_{carb}$ curves correlate to aragonite content, and there are no consistent geographic or water depth patterns (Figs. S9-S13). Although aragonite is most abundant during interglacials, it still comprises at least 10%, and typically ∼20–30%, of glacial samples (Figs. 5B and S14). Sr/Ca, which is high in aragonite (∼10–12 mmol/mol) and low in calcite (∼1 mmol/mol), follows the same trajectory as both aragonite content and $\delta^{13}C_{carb}$ (Fig. 5A).

3.2. *Co-variation between $\delta^{13}C_{carb}$, $\delta^{18}O_{carb}$, and mineralogy*

We evaluate the relationship between periplatform $\delta^{13}C_{carb}$ and $\delta^{18}O_{carb}$ during the Holocene, last glacial period, LIG, and pre-LIG (Fig. 6A). Note that the full LIG is not directly comparable to the Holocene because it captures the transition into the last glaciation, while the Holocene has not captured an analogous episode of sea level fall. However, we use the full data set in our analysis due to uncertainty in sample ages within the LIG. In the supplementary material, we show that excluding the latter portion of the LIG (∼120–115 ka) does not affect our results (Figs. S27 and S31).

LIG $\delta^{18}O_{carb}$ generally is higher than Holocene $\delta^{18}O_{carb}$ for samples with similar aragonite content (Fig. 6B), and mean $\delta^{18}O_{carb}$ is elevated by ∼0.6‰ during the LIG relative to the Holocene. A two-sample Kolmogorov-Smirnov test confirms that the LIG and Holocene $\delta^{18}O_{carb}$ data come from different distributions ($p < 0.01$), while a t-test confirms that the means of these distributions are different ($p < 0.01$). Notably, all samples with $\delta^{18}O_{carb}$ below −1‰ are from the Holocene. Considering the full data set, 3% of Holocene samples and 54% of LIG samples have $\delta^{18}O_{carb}$ greater than 0‰.

3.3. *Trace element concentrations and $\delta^{44/40}Ca$*

Trace element concentrations were measured for 45 Holocene, 55 last glacial period, 56 LIG, and 41 pre-LIG samples (Figs. 7A-L and S6-8). We focus on Sr/Ca, Mg/Ca, U/Ca, and Mn/Sr, which are predicted to change significantly during diagenesis due to mineralogy-, temperature-, and precipitation rate-dependent element partitioning. Note that mean Mg/Ca is 34.7 ± 10.6 ($\mu \pm 1\sigma$) mmol/mol during the Holocene and 27.1 ± 10.9 mmol/mol during the LIG, which reflects higher HMC content in Holocene samples ($19 \pm 4\%$) than in LIG samples ($12 \pm 6\%$). Measured $\delta^{44/40}Ca$ values ($n = 45$; Figs. 7M-N and S5-6) range from −1.58‰ in a LIG sample to −0.79‰ in a pre-LIG sample, with a mean of -1.24 ± 0.15‰.

3.4. *Clumped-isotope temperatures*

To test for secondary overprinting of initially warm formation temperatures in colder waters during burial (e.g., Staudigel and Swart, 2019), we measured clumped-isotope temperatures for 17 periplatform core samples, with 9 from the Holocene, 7 from the LIG, and 1 from the pre-LIG (Fig. 8). The pre-LIG sample has a clumped-isotope temperature of 7.0 ± 1.9 °C (1 s.e.), consistent with recrystallization in cold bottom waters. All other temperatures are potentially consistent with a primary origin (although minor diagenesis cannot be ruled out), with a mean of 21.7 ± 3.1 °C during the Holocene and 21.5 ± 2.8 °C (1σ) during the LIG. For comparison, the mean clumped-isotope temperature for banktop muds is 23.9 ± 1.8 °C ($n = 12$) (Geyman et al., 2022). Within individual cores, Holocene and LIG temperatures overlap within uncertainty (Fig. 8B). While Holocene and LIG temperatures are similar, mean $\delta^{18}O_{carb}$ is 0.57‰ higher and mean aragonite content is 14% higher in LIG samples. Holocene and LIG samples follow a similar relationship between $\delta^{18}O_{carb}$ and temperature, and least squares regressions overlap within uncertainty (Fig. 8C).

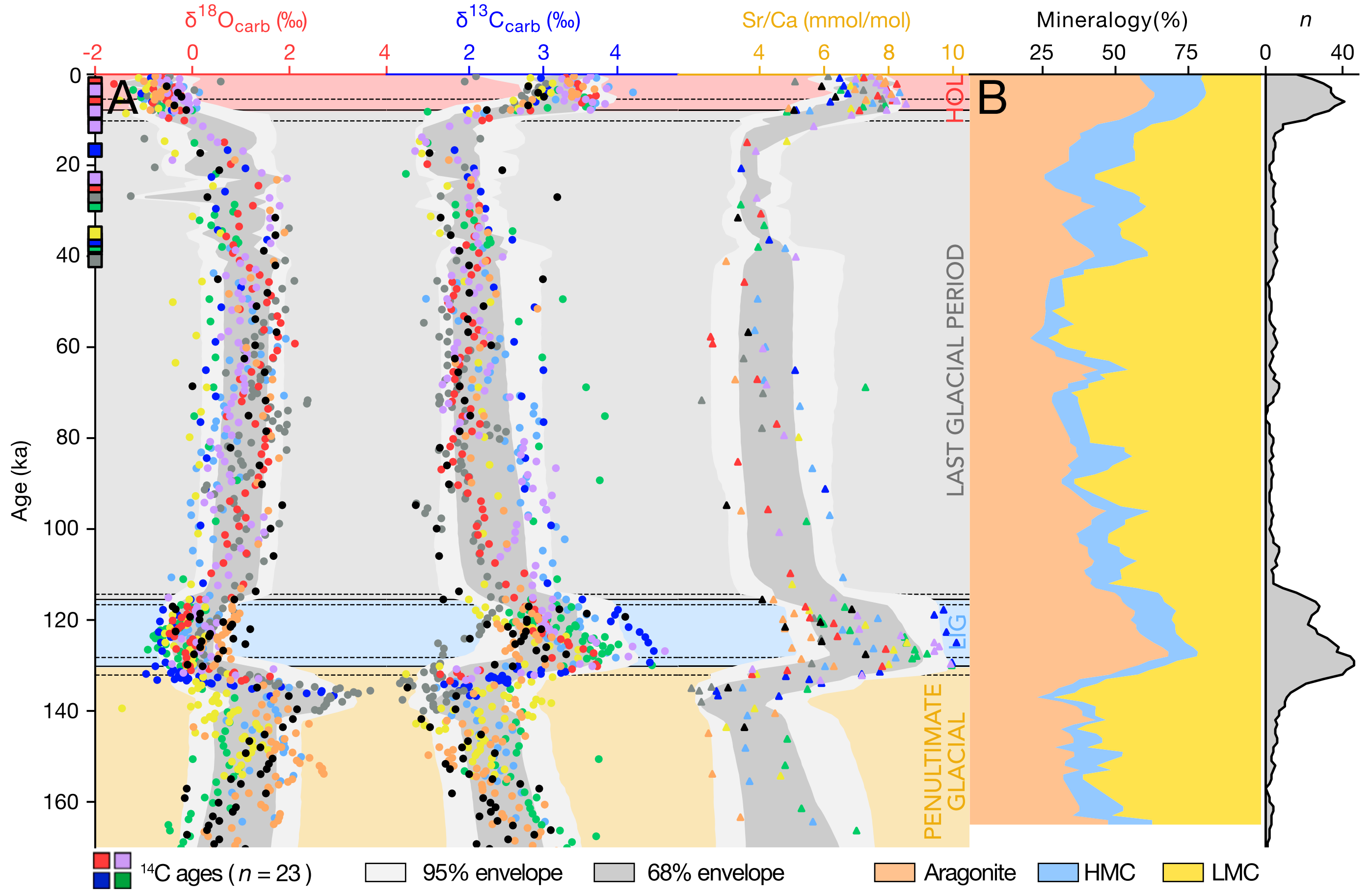

Fig. 5. A) $\delta^{18}O_{carb}$, $\delta^{13}C_{carb}$, and Sr/Ca stratigraphies for 9 periplatform cores aligned using our MCMC age models, which are based only on tie points in $\delta^{18}O_{carb}$ and ^{14}C age constraints. Colors correspond to individual cores as in Fig. 2. Data are plotted by median posterior age, and confidence envelopes are calculated using composite MCMC paths interpolated to a 1 kyr grid. ^{14}C age constraints (in calendar years B.P.) are plotted on the y-axis. B) Stack of periplatform core mineralogy. Mineralogy stratigraphies for individual cores are in Figs. S32 and S33. In B, each point represents the mean of at least $n = 3$ samples in a sliding 5 kyr window, with a mean sample size of $n = 10.7$. To the right, we show the number of samples within this sliding window.

3.5. *Thin section petrography*

All Holocene and LIG samples are wackestones with $83 \pm 2\%$ (1σ, $n = 11$) and $85 \pm 7\%$ ($n = 20$) mud, respectively. Last glacial period samples are slightly more shell-abundant wackestones, with $77 \pm 7\%$ ($n = 26$) mud. In all thin sections, the most abundant grain type is fine, broken-up skeletal fragments ($\mu = 11 \pm 3\%$, 1σ). More detailed point counting results are tabulated in section 2.1 of the supplementary material.

We do not observe petrographic evidence of fabric-destructive recrystallization or authigenic cement growth in any thin sections ($n = 88$), including 4 from samples that also have clumped isotope measurements (Fig. 8D-E). Therefore, if secondary cements or diagenetic fabrics are present, they are sub-micron in size and represent a small volume of the sample. While most large shells are well-preserved (Fig. 8E), some rare shells show evidence of minor dissolution (Fig. S5C-D).

3.6. *Sedimentation rates*

We assume that our identification of the Holocene and LIG age boundaries (section 2.11) in each core is correct, and use posterior MCMC sample ages for all paths ($n = 45{,}000$) to build Holocene and LIG sedimentation rate distributions for each core (Fig. S15). Mean sedimentation rate is 6.05 cm/kyr during the Holocene and 6.75 cm/kyr during the LIG, and LIG sedimentation rate is higher in 6 of 9 cores (Fig. S16). While limited in geographic extent, these data suggest the LIG platform may have exported more mud to the periplatform. Note that sedimentation rates must be calculated for the entire LIG because there are no intermediate tie points with absolute age constraints.

4. Discussion

Given similar tropical sea surface temperatures (Hoffman et al., 2017) and lower ice volume (Dutton and Lambeck, 2012) during the LIG, we would have predicted that the source marine water to the banktop would have had lower, rather than higher, $\delta^{18}O$ relative to the Holocene. That we observe the opposite signal suggests either that differences in local surface conditions and/or seawater chemistry increased primary $\delta^{18}O_{carb}$, or that secondary processes increased $\delta^{18}O_{carb}$ after deposition. Because post-depositional processes that change $\delta^{18}O_{carb}$ also can alter $\delta^{13}C_{carb}$, it is important to determine which process is driving the observed $\delta^{18}O_{carb}$ signal before answering the question of whether $\delta^{13}C_{carb}$ changed between the Holocene and LIG. Here, we present hypotheses for processes that could explain elevated LIG periplatform $\delta^{18}O_{carb}$. In Fig. 9, we evaluate hypotheses for post-depositional alteration in light of stable isotope, trace element, Δ_{47}, and mineralogy trends. After addressing the cause of elevated LIG $\delta^{18}O_{carb}$, we return to the question of whether changes in environmental boundary conditions between the LIG and Holocene changed banktop carbonate production and $\delta^{13}C$.

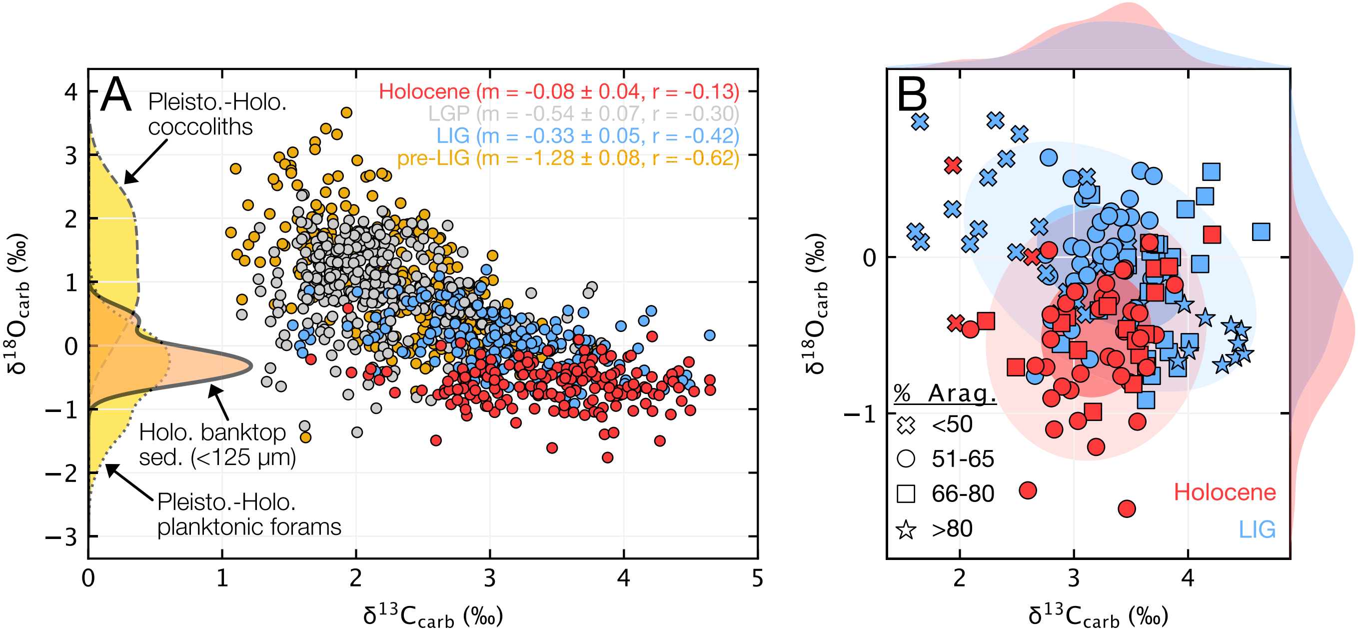

Fig. 6. A) $\delta^{13}C_{carb}$ and $\delta^{18}O_{carb}$ are negatively correlated in all periplatform core samples, and total least squares regression slopes are steeper during glacials than during interglacials. On the y-axis, we plot $\delta^{18}O$ distributions for major sediment sources to the periplatform. The Holocene banktop distribution includes the fine fraction of Recent Bahamian banktop sediment with high transport potential (Geyman and Maloof, 2021). The distribution for Pleistocene-Holocene planktonic foram $\delta^{18}O$ is based on data from cores collected around the Bahamas and the Caribbean Sea, while the coccolith $\delta^{18}O$ distribution includes data from a Caribbean core (Table S7). Coccolith $\delta^{18}O$ is elevated by 1–3‰ due to vital effects, where the magnitude of the vital effect increases as pCO_2 decreases (e.g., Hermoso, 2016). B) Here, we examine the subset of interglacial samples with mineralogy measurements. The Holocene and LIG populations occupy distinct but overlapping regions in $\delta^{18}O_{carb}$-$\delta^{13}C_{carb}$ space. Ellipses mark the 68% and 95% confidence envelopes for each population.

4.1. *Why is $\delta^{18}O_{carb}$ elevated in LIG samples?*

4.1.1. *Temperature and mineralogy*

Carbonate $\delta^{18}O$ is a function of both temperature and mineralogy (Fig. S18). Equilibrium $\delta^{18}O_{carb}$ increases by 0.2–0.25‰ for every 1 °C temperature decrease, and is ~0.8‰ higher for aragonite than for calcite produced under the same conditions (Kim et al., 2007). Regional sea surface temperatures likely were the same or slightly warmer during the LIG (Hoffman et al., 2017), which would decrease, rather than increase, $\delta^{18}O_{carb}$. For banktop carbonate, increasing aragonite content from 78%, the composition of our Recent banktop endmember (Fig. 3B), to 100% only elevates $\delta^{18}O_{carb}$ by 0.18‰. Therefore, the combined mineralogy and regional temperature levers might contribute to the observed signal, but can only explain a fraction of the ~0.6‰ elevation in LIG $\delta^{18}O_{carb}$.

4.1.2. *Mixing of primary sediment sources*

Since most LIG samples contain at least as much aragonite as Holocene samples, higher $\delta^{18}O_{carb}$ cannot be explained by increasing the relative abundance of coccolith calcite with high $\delta^{18}O$ (Figs. 3A and 6A). However, we cannot account for a possible shift in the distribution of different coccolith species. We also consider that mixing of different banktop aragonite sources could elevate $\delta^{18}O_{carb}$. To increase bulk sediment $\delta^{18}O_{carb}$ by 0.6‰, mean LIG aragonite $\delta^{18}O$ must be approximately +0.6‰, compared to −0.6‰ during the Holocene (Fig. S21). This scenario requires preferential export of aragonite with $\delta^{18}O$ above the 90th percentile for all Recent aragonite allochems (Fig. 3A), suggesting a major shift in source area. Therefore, while syndepositional mixing cannot be ruled out, we find this explanation unlikely.

We also test the hypothesis that LIG $\delta^{18}O_{carb}$ has been elevated through bioturbation, which could drive downward or upward mixing of glacial sediment into LIG sediment (Fig. S17A). Henderson et al. (1999) report bioturbation-driven sediment mixing to depths of ~8 cm on the slopes of the Little Bahama Bank. Globally, we calculate a mean mixing depth of 6.0 ± 4.0 cm for sediment deposited at water depths between 1000 and 3000 m (Solan et al., 2019). Because the thickness of the LIG sediment package in our cores is 100 ± 34 cm (Fig. S17B), bioturbation cannot account for elevated LIG $\delta^{18}O_{carb}$.

4.1.3. *Early marine diagenesis*

Next, we test the hypothesis that LIG $\delta^{18}O_{carb}$ was elevated during early marine diagenesis in deep, cold pore waters. We describe the expected behavior of key isotope and trace element systems during early marine diagenesis in section 2.8 of the supplementary material, and summarize our predictions in Fig. 9. The tight coupling between $\delta^{13}C_{carb}$, Sr/Ca, and aragonite content (Fig. 7A) is not consistent with neomorphism of aragonite to LMC. However, the reduction in both HMC content and Mg/Ca during the LIG (Figs. 7B and 9E-F) could be explained as preferential neomorphism of HMC to LMC (Fig. 9A) or dissolution of HMC (Droxler et al., 1988; Morse et al., 2006), which is consistent with rare petrographic evidence of dissolution (Fig. S5C-D). Depending on the $\delta^{18}O$ and temperature of the diagenetic fluids, which change during glacial cycles (Table S6), neomorphism of HMC to LMC could account for 0.20–0.31‰ of the observed ~0.6‰ bulk LIG $\delta^{18}O_{carb}$ increase (Fig. 9B). The magnitude of this effect also may be modulated by the rate of recrystallization, where $\delta^{18}O_{carb}$ increases as growth rate decreases (Watkins et al., 2014). Dissolution of HMC without subsequent reprecipitation as LMC only produces a 0.05‰ increase in bulk $\delta^{18}O_{carb}$ (Fig. 9D). These estimates assume that HMC comes from banktop *Peneroplis proteus* foraminifera; alternative assumptions are explored in section 2.8.2 of the supplementary material.

Geochemical and petrographic data suggest it is unlikely that early marine diagenesis is the primary process contributing to elevated LIG periplatform $\delta^{18}O_{carb}$. Excluding a single pre-LIG sample with high $\delta^{44/40}Ca$, our samples appear well-preserved with respect to both $\delta^{13}C_{carb}$ and $\delta^{44/40}Ca$ (Fig. 7M-N). Additionally, Sr/Ca and U/Ca have not been diagenetically reduced, and Mn/Sr has not been diagenetically enriched (Fig. 7). The absence of correlated changes in $\delta^{18}O_{carb}$ and concentrations of trace elements with mineralogy-dependent partition coefficients also indicates that significant recrystallization to

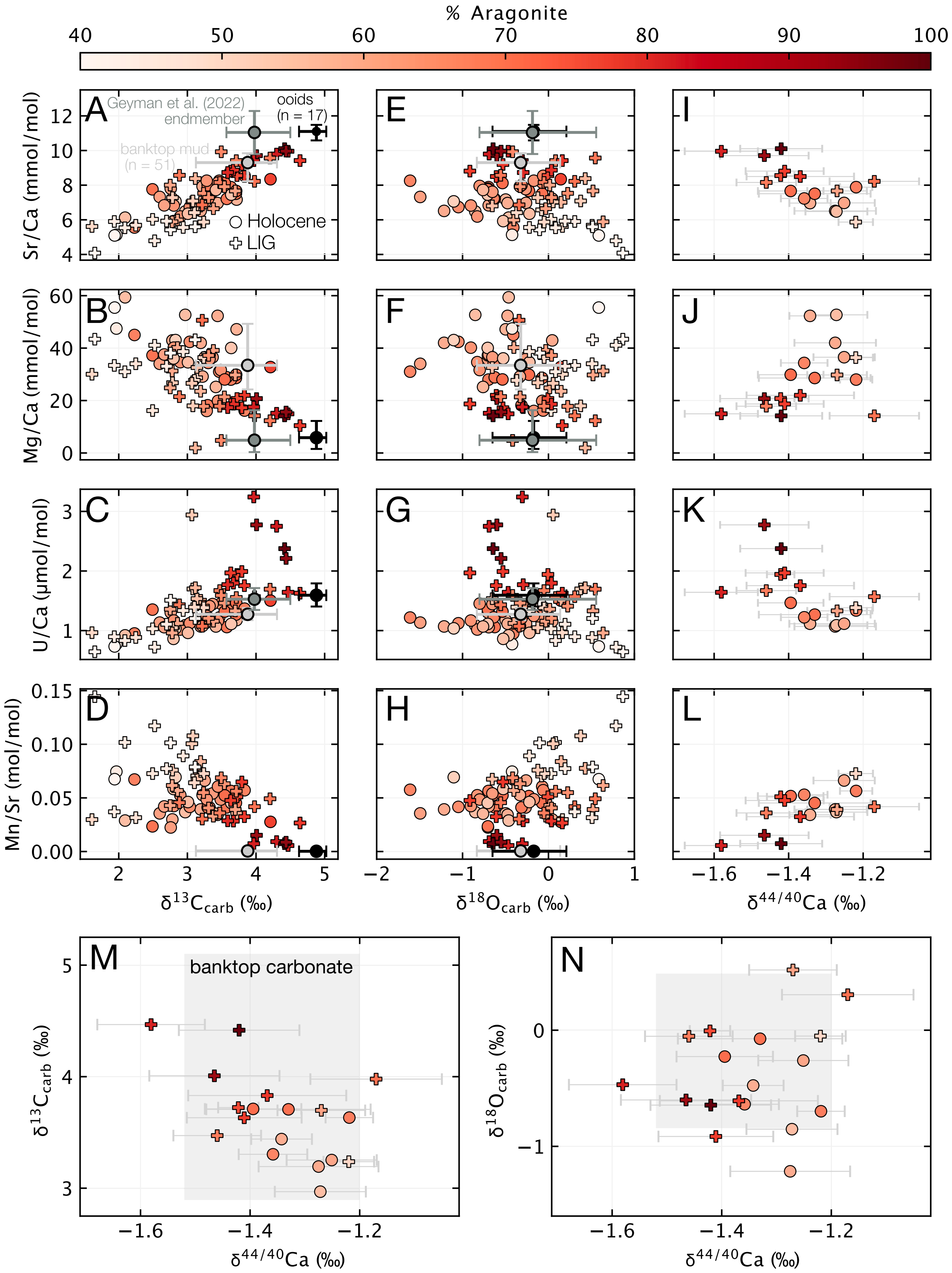

Fig. 7. We plot trace element concentrations against $\delta^{13}C_{carb}$ (A-D), $\delta^{18}O_{carb}$ (E-H), and $\delta^{44/40}$Ca (I-L). $\delta^{44/40}$Ca error bars are ±2 s.e. For comparison, we also plot the median compositions of banktop mud, ooids, and the inferred non-skeletal aragonite mud endmember from Geyman et al. (2022) with 5th and 95th percentiles. Data from glacial samples are in Figs. S6-S8. A) Interglacial Sr/Ca ranges from ~6 to 10 mmol/mol. B) Due to the difference in Mg concentrations between LMC (~5,000 ppm) and aragonite (~2,500 ppm), Mg/Ca decreases as $\delta^{13}C_{carb}$ and aragonite content increase. D) Mn/Sr is low in samples with high $\delta^{13}C_{carb}$ and aragonite content, and high in samples with low $\delta^{13}C_{carb}$ and aragonite content. E-L) There is no apparent structure to the relationships between $\delta^{18}O_{carb}$ or $\delta^{44/40}$Ca and Sr/Ca, Mg/Ca, U/Ca, or Mn/Sr during interglacials (glacial trends reflect mineralogical mixing; Fig. S6). M, N) Periplatform $\delta^{44/40}$Ca values for Holocene and LIG samples largely fall within the expected range for banktop carbonate, based on measurements of mud from around NW Andros Island and ooids from Joulter Cays (−1.36 ± 0.16‰; Higgins et al., 2018). Banktop $\delta^{13}C_{carb}$ and $\delta^{18}O_{carb}$ ranges are based on the exported banktop endmember defined in Fig. 3B.

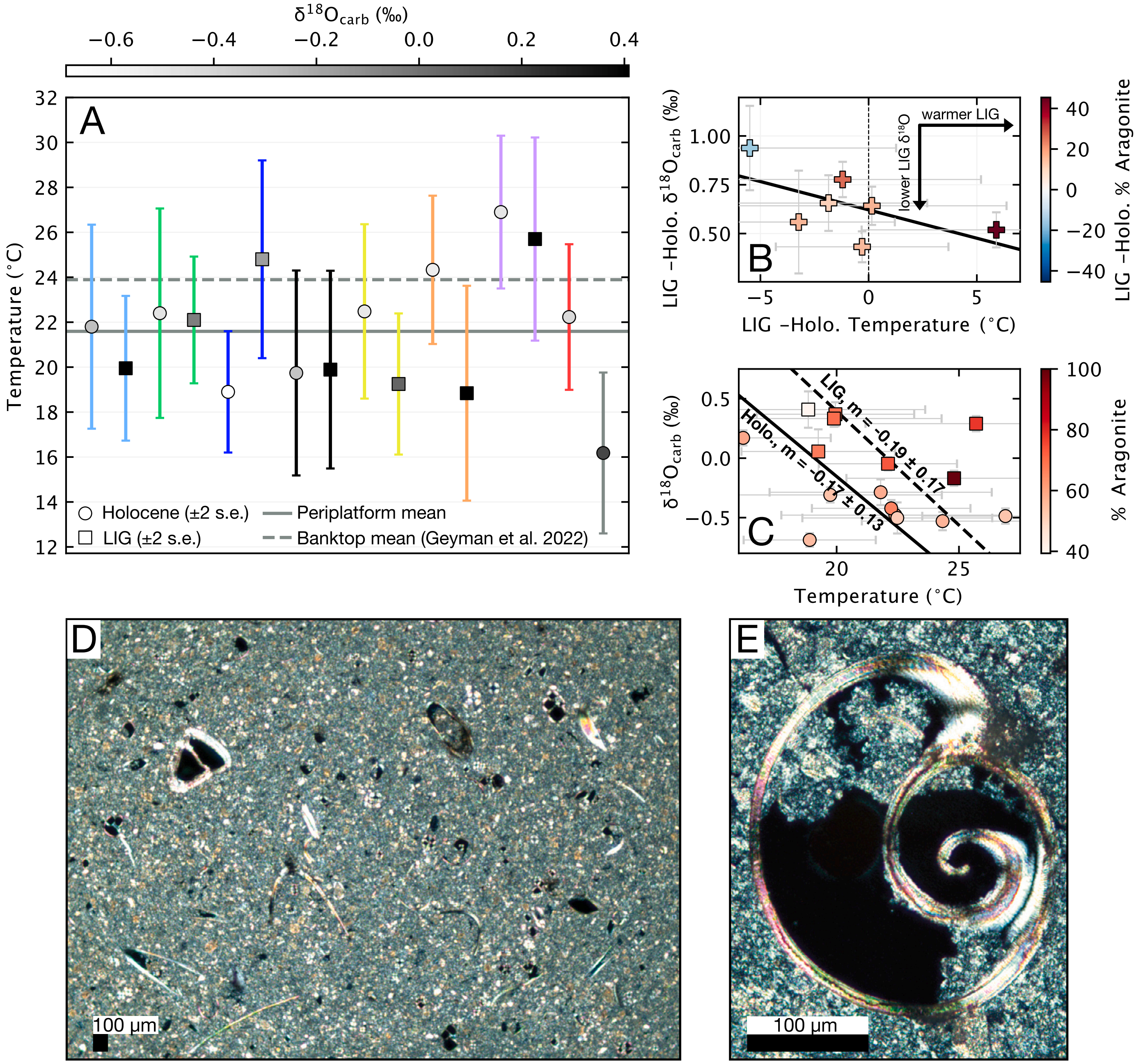

Fig. 8. A) Clumped-isotope temperatures for Holocene and LIG periplatform core samples. Marker grayscale tracks sediment δ^{18}O, while error bar colors correspond to individual cores as in Fig. 2. B) For cores with both Holocene and LIG clumped-isotope temperatures, we examine LIG-Holocene differences in temperature, $\delta^{18}O_{carb}$, and aragonite content. C) Least squares regressions through Holocene and LIG $\delta^{18}O_{carb}$ and temperature data. Note that we do not plot the diagenetically altered pre-LIG sample that yielded a temperature of 7.0 ± 2.0 °C (1 s.e.). D) Example of a typical interglacial wackestone under cross-polarized light. This sample (VM06011-210) is from the LIG, and has a clumped-isotope temperature of 19.3 ± 1.6 °C (1 s.e.). A point count ($n = 500$) of this sample reveals 81% carbonate mud, 13% fine skeletal fragments, and 6% larger shell fragments that include gastropods, foraminifera, bivalves, and corals. We observe no cements on the >10 micron scale. E) A well-preserved gastropod from LIG sample AT167048-168, which has a clumped-isotope temperature of 24.8 ± 2.2 °C (1 s.e.). The shell is partly filled with sediment and shows no evidence of cement growth. Scale bars are 100 microns.

LMC has not occurred. Since diagenesis in cold bottom waters is predicted to reduce clumped-isotope temperatures, close agreement between Holocene and LIG clumped-isotope temperatures (Fig. 8A-C) further suggests little to no diagenesis. Finally, the absence of cements or diagenetic fabrics in LIG thin sections indicates these samples are well-preserved.

4.1.4. Aragonite cement formation

Next, we consider that precipitation of an open-system authigenic aragonite cement (e.g., Grammer et al., 1993) in the pore space could raise $\delta^{18}O_{carb}$ without increasing LMC content. This hypothesis is consistent with LIG aragonite content that frequently exceeds the maximum Holocene value of 76% (Figs. 7 and S31), and does not require us to assume that initial LIG periplatform mineralogy was identical to the Holocene. For cement formation contemporaneous with deposition (e.g., in LIG bottom waters), the observed $\delta^{18}O_{carb}$ is best explained if 13% of the aragonite in our LIG samples is a secondary cement and 87% was sourced from the banktop (Fig. 9C). If cement formation instead occurred under glacial conditions, then 11% of the aragonite in our LIG samples must be cement (Fig. S22).

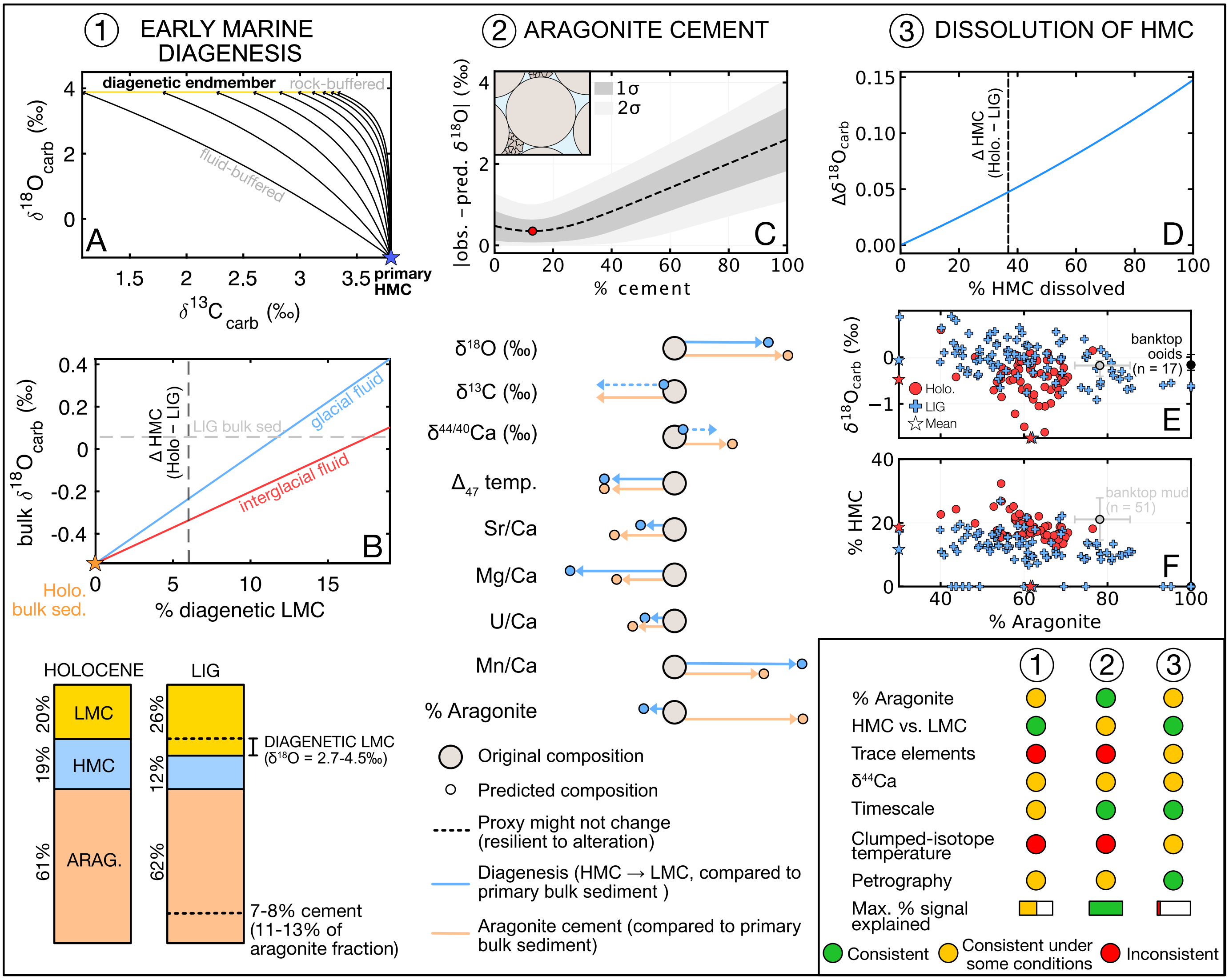

Fig. 9. We test three hypotheses for post-depositional processes that could explain elevated LIG periplatform $\delta^{18}O_{carb}$. In all experiments, we assume that LIG bulk sediment initially had the same $\delta^{18}O$ as Holocene bulk sediment. Hypothesis 1 suggests that neomorphism of HMC to LMC during early marine diagenesis increased LIG $\delta^{18}O_{carb}$. In A, we plot diagenetic trajectories for recrystallization of the HMC endmember in glacial seawater (Table S6) under a range of open- to closed-system conditions (Ahm et al., 2018). In B, we show the predicted bulk $\delta^{18}O_{carb}$ for different abundances of diagenetic LMC under both glacial and interglacial fluid conditions. Hypothesis 2 suggests that authigenic aragonite cement growth increased LIG $\delta^{18}O_{carb}$. Panel C shows the residual between measured and predicted LIG bulk $\delta^{18}O_{carb}$ for different cement fractions assuming growth in interglacial seawater; the red circle marks the optimal solution. Schematic directional arrows illustrate predicted isotope and trace element fingerprints for both early marine diagenesis and aragonite cement growth. Arrows show the approximate magnitude and direction of the expected change relative to the original bulk sediment. Finally, Hypothesis 3 suggests that preferential dissolution of HMC could elevate $\delta^{18}O_{carb}$. In D, we predict the bulk sediment $\delta^{18}O_{carb}$ increase caused by dissolution. Data in E and F illustrate the LIG elevation in $\delta^{18}O$ and depletion in HMC content relative to the Holocene. The bottom right panel summarizes the agreement of each hypothesis with our geochemical data, petrographic observations, and physical constraints on deposition.

Authigenic cements are not visible in LIG thin sections, and must be interstitial and sub-micron in size if present (Fig. 8D-E). However, combined isotope and trace element data suggest it is unlikely that our samples contain interstitial aragonite cements. First, cement growth in deep, cold pore waters would lower LIG clumped-isotope temperatures; in our data, LIG and Holocene clumped-isotope temperatures are not significantly different (Fig. 8A-C). An open-system authigenic aragonite cement also would have lower $\delta^{13}C$, higher $\delta^{44/40}Ca$, and lower Sr/Ca, Mg/Ca, and U/Ca than banktop aragonite due to temperature- and rate-dependent element partitioning in cooler bottom waters (Fig. 9; e.g., Gussone et al., 2020; Lorens, 1981; Gabitov et al., 2008). In our data, the tight linear relationship between Sr/Ca, $\delta^{13}C_{carb}$, and aragonite content (Fig. 7A), and the strong overlap between LIG periplatform $\delta^{44/40}Ca$ and banktop endmember $\delta^{44/40}Ca$ (Fig. 7M-N) all suggest that LIG aragonite is mostly or entirely sourced from the banktop.

4.1.5. *How were local climate and environment different during the LIG?*

Since $\delta^{18}O_{carb}$ has not been diagenetically altered, we can use the offset in $\delta^{18}O_{carb}$ between the Holocene and LIG to make inferences about local LIG climate and environment. Geochemical fingerprinting does not allow us to confidently differentiate between different primary levers on periplatform $\delta^{18}O_{carb}$, and the observed signal likely represents the combined effects of multiple processes. However, we outline the interpretations that we find most likely based on agreement with independent proxy data:

- **Source water chemistry:** LIG $\delta^{18}O_{carb}$ may have been increased by raising the $\delta^{18}O$ of open-marine source waters advected onto the banktop. While there is no consistent $\delta^{18}O$ offset in planktonic foraminifera from 5 nearby cores (Table S7), planktonic $\delta^{18}O$ is 0.01 − 0.48‰ higher during the LIG, suggesting open-marine source water chemistry may contribute to the observed signal. Many different oceanographic processes could change regional open-ocean $\delta^{18}O$ (e.g., LeGrande and Schmidt, 2006); identifying the likely cause is beyond the scope of this study.
- **Sea level:** Differences in local sea level between the Holocene and LIG (Figure S24; Dyer et al., 2021) likely shifted the organization of banktop environments (e.g., Beach and Ginsburg, 1980; Kindler and Hearty, 1996; Hearty, 1998). Associated changes in banktop circulation and restriction may have raised the average $\delta^{18}O$ of banktop waters ($\delta^{18}O_{banktop}$). In addition, subsidence likely generated ∼2 m of accommodation space between the end of the LIG and the start of the Holocene, compared to ∼5–6 m between MIS 11 (the previous highstand with global-mean sea level similar to today; Dutton et al., 2015) and the start of the LIG (assuming 2 m of subsidence per 100 kyr; Lynts, 1970). Therefore, more accommodation space likely was available at the start of the LIG, and average banktop waters may have been slightly deeper and cooler.

  Andros Island also may have experienced uplift throughout the LIG and subsidence throughout the Holocene because the ice load on North America was smaller prior to the LIG than during the LGM (Dyer et al., 2021). Net uplift (or lower net subsidence) during the LIG could reduce accommodation space over time, decreasing the fraction of mud trapped in tidal flats on the leeward side of Andros (e.g., Purkis and Harris, 2016) and increasing off-shelf export. However, on the modern Great Bahama Bank, the increase in $\delta^{18}O_{banktop}$ from evaporative enrichment is counterbalanced by temperature-dependent fractionation in warmer banktop waters, which decreases $\delta^{18}O_{carb}$. As a result, carbonates from restricted environments have the same $\delta^{18}O$ as bank-margin mud (Geyman et al., 2022). Therefore, an increase in $\delta^{18}O_{carb}$ requires increasing evaporative enrichment without raising water temperature.
- **Aridity:** Enhanced evaporative enrichment and/or reduced input of low-$\delta^{18}O$ meteoric waters in a locally more arid climate could increase $\delta^{18}O_{banktop}$ without necessarily increasing temperature, raising the $\delta^{18}O$ of banktop carbonate exported to the periplatform. Larger-than-modern LIG aeolian parabolic dunes (Kindler and Strasser, 2000; Vimpere et al., 2021) provide geologic evidence of enhanced aridity in the Bahamas during at least part of the LIG (although the origin of these dunes has been debated; see e.g., Hearty et al., 2000). While parabolic dunes are observed in the LIG record, they are absent in the modern Bahamas due to some combination of decreased sand supply, increased moisture (stabilization by vegetation and cementation preventing landward dune migration), and antecedent topography from LIG dunes blocking sand migration. Higher aridity also is consistent with LIG climate models predicting reduced regional precipitation (e.g., Scussolini et al., 2019).

4.2. Was the $\delta^{13}C_{carb}$ of banktop mud different during the LIG?

Given both elevated $\delta^{18}O_{carb}$ and independent physical indicators, such as sea level and parabolic dune formation, it is clear that local environment and climate were different during the LIG. Since we have shown that primary $\delta^{13}C_{carb}$ is well-preserved, we now can evaluate whether these differences in environment altered the average $\delta^{13}C$ of LIG banktop carbonate. We use paired measurements of periplatform $\delta^{13}C_{carb}$ and mineralogy to estimate the $\delta^{13}C$ of each mineralogical endmember during the Holocene, last glacial period, and LIG following the methodology outlined in section 2.10 (reported estimates are $\mu \pm 2\sigma$; Figs. 10 and S25-27). The optimal aragonite endmember $\delta^{13}C$ is 4.68 ± 0.24‰ during the LIG, compared to 4.63 ± 0.67‰ for the Holocene. Despite observed changes to $\delta^{18}O_{carb}$, surface conditions, and shelfal export, the average $\delta^{13}C$ of exported aragonite remained constant. In other words, the $\delta^{13}C$ of average banktop export appears insensitive to differences in climate and environment between the LIG and the Holocene.

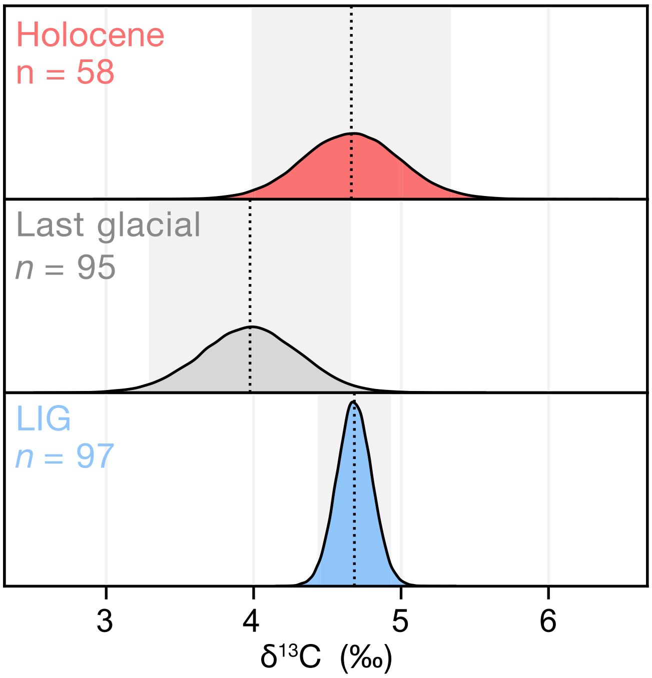

Fig. 10. Posterior $\delta^{13}C$ distributions for the calculated Holocene, last glacial period, and LIG aragonite endmembers are plotted with mean and 2σ uncertainty. Posterior distributions for the $\delta^{13}C$ of HMC and LMC are in Fig. S25.

4.3. Was the source area of banktop mud delivered to the periplatform different during the LIG?

To explore the implications of constant $\delta^{13}C$, we first must understand where exported banktop carbonate is formed, and whether this source area changed between the LIG and the Holocene. Geyman et al. (2022) used geochemical fingerprinting to show that most aragonite mud on the modern Great Bahama Bank comes from non-skeletal precipitation in the water column (e.g., Milliman et al., 1993), where mud production peaks on the bank margins (Broecker and Takahashi, 1966). Geyman et al. (2022) inferred that this non-skeletal mud has a $\delta^{13}C$ of 3.99 ± 0.57‰, which is 0.64‰ lower than our inferred Holocene periplatform aragonite endmember (Fig. 10). This offset suggests either that the $\delta^{13}C$ of bank-margin aragonite mud varies across the archipelago, or that aragonite exported to the periplatform is a mix of bank-margin mud and material with elevated $\delta^{13}C_{carb}$ derived from the banktop interior (e.g., from whitings; Purkis et al., 2017, 2023). Note that mixing of bank-margin and bank-interior sources is compatible with sea level and/or aridity influencing $\delta^{18}O_{carb}$ (section 4.1.5).

Our periplatform clumped-isotope temperatures are consistent with mixing between bank-margin and bank-interior sources. Holocene clumped-isotope temperatures range from 16.2 ± 1.8 °C to 26.9 ± 1.7 °C (1 s.e.), with the highest and lowest points not overlapping within ±2 s.e., and with two temperatures above 24 °C from cores VM07-015 and VM07-016 (Fig. 8A). Given that all Holocene samples with clumped-isotope measurements have similar aragonite content (56 ± 4%), differences in temperature cannot be explained by mineralogy. Instead, disparate formation temperatures likely indicate the carbonate in each core was sourced from different regions and/or water depths. For example, VM07-015 is located near the margin of the Little Bahama Bank (Fig. 2), and likely receives a greater amount of exported bank-interior sediment than more distal cores. Similarly, the warm clumped-isotope temperature from VM07-016, located in the northern Tongue of the Ocean (TOTO; Fig. 2), may reflect input of banktop-derived carbonate from the platform north of Andros Island. In contrast, cooler clumped-isotope temperatures ($\mu = 21.0 \pm 1.5\,^{\circ}\mathrm{C}$, 1σ) from cores AT167-046, AT167-047, and AT167-048 could record export from a narrower and deeper area of mud production east of Andros Island, where shallow catchment area is more limited, and/or mixing between mud sourced from the eastern and western margins of the TOTO. Cores AT179-013 and AT179-014 also have limited shallow catchment area (located in the Exuma Sound basin and on the windward margin of the archipelago, respectively; Fig. 2) and low Holocene clumped-isotope temperatures.

Our data suggest the source region of exported mud generally was similar during the LIG. First, Holocene and LIG clumped-isotope temperatures within each core overlap within ±2 s.e., indicating no significant change in the average water temperature of the source area. In addition, the δ^{13}C of aragonite mud largely is a function of source area, where bank-interior aragonite has higher δ^{13}C than bank-margin aragonite (Swart et al., 2009; Geyman et al., 2022). Therefore, constant δ^{13}C of periplatform aragonite (Fig. 10) indicates that the average source area of exported aragonite did not change. Given similar source area, we posit that constant periplatform aragonite δ^{13}C between the LIG and the Holocene simply reflects 1) constant $\delta^{13}C_{DIC}$ of source marine waters advected onto the banktop, and 2) no significant change in average carbon cycling across the archipelago.

4.4. Does aragonite mud production persist during sea level lowstands?

The last glacial period aragonite endmember has a δ^{13}C of 3.95 ± 0.67‰, representing a mean depletion of 0.68‰ relative to the Holocene (Fig. 10). Glacial samples follow the same relationship between Sr/Ca and aragonite content as Holocene samples (Fig. S29), which is inconsistent with a glacial increase in the relative abundance of low-Sr aragonite from pelagic gastropods and benthic mollusks (Boardman and Neumann, 1984). Furthermore, thin section point counts suggest that gastropods are only slightly more abundant during the last glacial period ($1.7 \pm 1.5\%$, 1σ; $n = 26$) compared to the Holocene ($0.7 \pm 0.6\%$, 1σ; $n = 11$). Lower glacial δ^{13}C more likely represents continued production of aragonite mud on the upper slopes during lowstands (Boardman et al., 1986; Geyman et al., 2022), where δ^{13}C is lower either due to a glacial decrease in global-mean $\delta^{13}C_{DIC}$ (e.g., Curry et al., 1988), or because $\delta^{13}C_{DIC}$ is not as elevated by photosynthesis in restricted waters.

Models that assume the shallow carbonate factory shuts down when the banktop is subaerially exposed during lowstands (Opdyke and Walker, 1992) predict a significant increase in deep-sea carbonate preservation during glacials that is not supported by observations (Catubig et al., 1998). If shallow carbonate burial persists on the periplatformal slopes during lowstands, then the compensatory increase in deep-sea carbonate burial required to balance alkalinity flux to the oceans is reduced, potentially contributing to glacial-interglacial stability of the carbonate compensation depth (Opdyke and Walker, 1992; Catubig et al., 1998; Geyman et al., 2022).

4.5. Implications for shallow δ^{13}C chemostratigraphy

Parasequence-scale shifts in $\delta^{13}C_{carb}$ frequently are interpreted as changes in $\delta^{13}C_{DIC}$ related to global or regional phenomena such as glacioeustasy and nutrient cycling (e.g., Ludvigson et al., 2004; Cramer and Saltzman, 2005; Melchin and Holmden, 2006). However, we have shown that the δ^{13}C of exported aragonite mud did not change between the LIG and Holocene (Fig. 10), which indicates that local-mean carbon cycling and $\delta^{13}C_{DIC}$ remained constant despite perturbations to both global climate and regional environment. In contrast, bulk $\delta^{13}C_{carb}$ varies by ~5‰ between different coeval environments on the modern banktop (Geyman and Maloof, 2021). Together, these observations suggest that, at least in a Pleistocene Bahamas framework, shifts in $\delta^{13}C_{carb}$ that occur on short stratigraphic lengthscales (i.e., within and between meter-scale parasequences; Fig. S30) may be related to facies or diagenesis.

4.6. Periplatform records as paleoclimate archives

Our results also illustrate the potential importance of ancient periplatform stratigraphies (e.g., Pujalte et al., 1998; Pittet et al., 2000) as paleoclimate archives. For instance, periplatform sections are crucial for studying carbon cycling during the Carboniferous (Campion et al., 2018) because banktop records were subaerially exposed and overprinted by meteoric diagenesis during the Late Paleozoic Ice Age (Dyer et al., 2015). The periplatform is useful even when shallow stratigraphies are well-preserved because it acts as a low-pass filter, providing a way to see signal through the 'noise' of facies changes and cross-shelf geochemical gradients on the shallow banktop. On platforms with carbonate factories analogous to the modern Bahamas, where mud production persists on the slopes during sea level lowstands, periplatform stratigraphies also may record continuous deposition of both pelagic (after the mid-Mesozoic; Ridgwell, 2005) and non-skeletal carbonate mud during hiatuses on the banktop.

5. Conclusions

Using combined measurements of $\delta^{13}C_{carb}$, $\delta^{18}O_{carb}$, $\delta^{44/40}$Ca, mineralogy, trace element concentrations, and Δ_{47} from Bahamian periplatform cores, we have demonstrated that average banktop $\delta^{13}C_{carb}$ remained constant between the LIG and the Holocene despite differences in sea level, climate, and local banktop environment. In contrast, bulk $\delta^{13}C_{carb}$ is highly variable across the modern banktop (Geyman and Maloof, 2021). Together, these observations suggest that local influences on $\delta^{13}C_{carb}$, such as facies and diagenesis, must be ruled out before attributing parasequence-scale stratigraphic shifts in shallow-water $\delta^{13}C_{carb}$ to changing global or local-mean $\delta^{13}C_{DIC}$.

This study also illustrates that periplatform records, where available, serve as important complements to banktop records. First, the periplatform records continued sedimentation during sea level lowstands, rather than a hiatus and erosion. Second, periplatform geochemistry is not complicated by meteoric diagenesis or localized facies changes. Third, our results suggest it might be possible to tease out subtle differences between interglacials by studying changes in periplatform bed and cycle thicknesses. In light of these advantages, we suggest that studies of farfield records from periods of Earth history marked by glaciations should, when possible, incorporate observations from both shallow and periplatform environments.

CRediT authorship contribution statement

Stacey Edmonsond: Writing – original draft, Visualization, Methodology, Investigation, Formal analysis, Conceptualization. **Matthew D. Nadeau:** Writing – review & editing, Investigation. **Andrew C. Turner:** Writing – review & editing, Investigation. **Ziman Wu:** Writing – review & editing, Investigation. **Emily C. Geyman:** Writing – review & editing, Investigation. **Anne-Sofie C. Ahm:** Writing – review & editing, Methodology. **Blake Dyer:** Writing – review & editing, Methodology. **Sergey Oleynik:** Writing – review & editing, Resources. **David McGee:** Writing – review & editing, Resources. **Daniel A. Stolper:** Writing – review & editing, Resources. **John A. Higgins:** Writing – review & editing, Resources. **Adam C. Maloof:** Writing – review & editing, Supervision, Resources, Conceptualization.

Declaration of competing interest

The authors declare that they have no known competing financial interests or personal relationships that could have appeared to influence the work reported in this paper.

Data availability

All data and code required to reproduce our analysis are available on GitHub (https://github.com/sedmonsond/bahamas-periplatform-epsl) and Zenodo (https://doi.org/10.5281/zenodo.10211822).

Acknowledgements

We would like to thank Nichole Anest and Mallory Mintz at the Lamont-Doherty Core Repository of Lamont-Doherty Earth Observatory for their hospitality and assistance while collecting the samples used in this study, and Maureen Raymo for opening the core repository to us. Thank you to Kathryn Elder and the laboratory staff at NOSAMS for performing radiocarbon analyses. Additionally, we thank Ryan Manzuk, Sarah Ward, Stefania Gili, Daniel Gregory, John Schreiber, and Nan Yao for assistance with laboratory work. We acknowledge the use of Princeton's Imaging and Analysis Center (IAC), which is partially supported through the Princeton Center for Complex Materials (PCCM), a National Science Foundation (NSF)-MRSEC program (DMR-2011750). S.E. acknowledges support from the Princeton Geosciences Department, the Princeton Department of Undergraduate Research, and the Evolving Earth Foundation. D.A.S. acknowledges support from the U.S. Department of Energy, Office of Science, Office of Basic Energy Sciences, Chemical Sciences, Geosciences, and Biosciences Division, under Award Number DE-AC02-05CH11231.

Appendix A. Supplementary material

Supplementary material related to this article can be found online at https://doi.org/10.1016/j.epsl.2023.118566.

References

Abril-Pla, O., Adreani, V., Carroll, C., Dong, L., Fonnesbeck, C.J., Kochurov, M., Kumar, R., Lao, J., Luhmann, C.C., Martin, O.A., Osthege, M., Vieira, R., Wiecki, T., Zinkov, R., 2023. PyMC: a modern and comprehensive probabilistic programming framework in Python. PeerJ Comput. Sci. 9, e1516. https://doi.org/10.7717/peerj-cs.1516.

Ahm, A.-S.C., Bjerrum, C.J., Blättler, C.L., Swart, P.K., Higgins, J.A., 2018. Quantifying early marine diagenesis in shallow-water carbonate sediments. Geochim. Cosmochim. Acta 236, 140–159. https://doi.org/10.1016/j.gca.2018.02.042.

Ahm, A.-S.C., Bjerrum, C.J., Hoffman, P.F., Macdonald, F.A., Maloof, A.C., Rose, C.V., Strauss, J.V., Higgins, J.A., 2021. The Ca and Mg isotope record of the Cryogenian Trezona carbon isotope excursion. Earth Planet. Sci. Lett. 568, 117002. https://doi.org/10.1016/j.epsl.2021.117002.

Allan, J., Matthews, R., 1982. Isotope signatures associated with early meteoric diagenesis. Sedimentology 29, 797–817. https://doi.org/10.1002/9781444304510.ch16.

Anderson, N.T., Kelson, J.R., Kele, S., Daëron, M., Bonifacie, M., Horita, J., Mackey, T.J., John, C.M., Kluge, T., Petschnig, P., Jost, A.B., Huntington, K.W., Bernasconi, S.M., Bergmann, K.D., 2021. A unified clumped isotope thermometer calibration (0.5–1, 100°C) using carbonate-based standardization. Geophys. Res. Lett. 48, e2020GL092069. https://doi.org/10.1029/2020GL092069.

Andres, M.S., Sumner, D.Y., Reid, R.P., Swart, P.K., 2006. Isotopic fingerprints of microbial respiration in aragonite from Bahamian stromatolites. Geology 34, 973–976. https://doi.org/10.1130/G22859A.1.

Beach, D.K., Ginsburg, R.N., 1980. Facies succession of Pliocene-Pleistocene carbonates, northwestern Great Bahama Bank. AAPG Bull. 64, 1634–1642. https://doi.org/10.1306/2F9196D9-16CE-11D7-8645000102C1865D.

Bengtson, S.A., Menviel, L.C., Meissner, K.J., Missiaen, L., Peterson, C.D., Lisiecki, L.E., Joos, F., 2021. Lower oceanic δ^{13}C during the last interglacial period compared to the Holocene. Clim. Past 17, 507–528. https://doi.org/10.5194/cp-17-507-2021.

Boardman, M.R., Neumann, A.C., 1984. Sources of periplatform carbonates; Northwest Providence Channel, Bahamas. J. Sediment. Res. 54, 1110–1123. https://doi.org/10.1306/212F8571-2B24-11D7-8648000102C1865D.

Boardman, M.R., Neumann, A.C., Baker, P.A., Dulin, L.A., Kenter, R.J., Hunter, G.E., Kiefer, K.B., 1986. Banktop responses to Quaternary fluctuations in sea level recorded in periplatform sediments. Geology 14, 28–31. https://doi.org/10.1130/0091-7613(1986)14<28:BRTQFI>2.0.CO;2.

Broecker, W.S., Takahashi, T., 1966. Calcium carbonate precipitation on the Bahama Banks. J. Geophys. Res. 71, 1575–1602. https://doi.org/10.1029/JZ071i006p01575.

Burkhardt, S., Riebesell, U., Zondervan, I., 1999. Effects of growth rate, CO_2 concentration, and cell size on the stable carbon isotope fractionation in marine phytoplankton. Geochim. Cosmochim. Acta 63, 3729–3741. https://doi.org/10.1016/S0016-7037(99)00217-3.

Campion, A., Maloof, A., Schoene, B., Oleynik, S., Sanz-López, J., Blanco-Ferrera, S., Merino-Tomé, O., Bahamonde, J.R., Fernández, L.P., 2018. Constraining the timing and amplitude of early Serpukhovian glacioeustasy with a continuous carbonate record in northern Spain. Geochem. Geophys. Geosyst. 19, 2647–2660. https://doi.org/10.1029/2017GC007369.

Catubig, N.R., Archer, D.E., Francois, R., deMenocal, P., Howard, W., Yu, E.-F., 1998. Global deep-sea burial rate of calcium carbonate during the Last Glacial Maximum. Paleoceanography 13, 298–310. https://doi.org/10.1029/98PA00609.

Cramer, B.D., Saltzman, M.R., 2005. Sequestration of ^{12}C in the deep ocean during the early Wenlock (Silurian) positive carbon isotope excursion. Palaeogeogr. Palaeoclimatol. Palaeoecol. 219, 333–349. https://doi.org/10.1016/j.palaeo.2005.01.009.

Curry, W.B., Duplessy, J.C., Labeyrie, L.D., Shackleton, N.J., 1988. Changes in the distribution of δ^{13}C of deep water ΣCO_2 between the Last Glaciation and the Holocene. Paleoceanography 3, 317–341. https://doi.org/10.1029/PA003i003p00317.

Droxler, A.W., Morse, J.W., Kornicker, W.A., 1988. Controls on carbonate mineral accumulation in Bahamian basins and adjacent Atlantic Ocean sediments. J. Sediment. Res. 58, 120–130. https://doi.org/10.1306/212F8D2D-2B24-11D7-8648000102C1865D.

Dutton, A., Carlson, A.E., Long, A.J., Milne, G.A., Clark, P.U., DeConto, R., Horton, B.P., Rahmstorf, S., Raymo, M.E., 2015. Sea-level rise due to polar ice-sheet mass loss during past warm periods. Science 349, aaa4019. https://doi.org/10.1126/science.aaa4019.

Dutton, A., Lambeck, K., 2012. Ice volume and sea level during the last interglacial. Science 337, 216–219. https://doi.org/10.1126/science.1205749.

Dyer, B., Austermann, J., D'Andrea, W.J., Creel, R.C., Sandstrom, M.R., Cashman, M., Rovere, A., Raymo, M.E., 2021. Sea-level trends across The Bahamas constrain peak last interglacial ice melt. Proc. Natl. Acad. Sci. 118. https://doi.org/10.1073/pnas.2026839118.

Dyer, B., Maloof, A.C., Higgins, J.A., 2015. Glacioeustasy, meteoric diagenesis, and the carbon cycle during the Middle Carboniferous. Geochem. Geophys. Geosyst. 16, 3383–3399. https://doi.org/10.1002/2015GC006002.

Gabitov, R., Gaetani, G., Watson, E., Cohen, A., Ehrlich, H., 2008. Experimental determination of growth rate effect on U^{6+} and Mg^{2+} partitioning between aragonite and fluid at elevated U^{6+} concentration. Geochim. Cosmochim. Acta 72, 4058–4068. https://doi.org/10.1016/j.gca.2008.05.047.

Geyman, E.C., Maloof, A.C., 2019. A diurnal carbon engine explains ^{13}C-enriched carbonates without increasing the global production of oxygen. Proc. Natl. Acad. Sci. 116, 24433–24439. https://doi.org/10.1073/pnas.1908783116.

Geyman, E.C., Maloof, A.C., 2021. Facies control on carbonate δ^{13}C on the Great Bahama Bank. Geology 49, 1049–1054. https://doi.org/10.1130/G48862.1.

Geyman, E.C., Wu, Z., Nadeau, M.D., Edmonsond, S., Turner, A., Purkis, S.J., Howes, B., Dyer, B., Ahm, A.-S.C., Yao, N., Deutsch, C.A., Higgins, J.A., Stolper, D.A., Maloof, A.C., 2022. The origin of carbonate mud and implications for global climate. Proc. Natl. Acad. Sci. 119, e2210617119. https://doi.org/10.1073/pnas.2210617119.

Ghosh, P., Adkins, J., Affek, H., Balta, B., Guo, W., Schauble, E.A., Schrag, D., Eiler, J.M., 2006. ^{13}C–^{18}O bonds in carbonate minerals: a new kind of paleothermometer. Geochim. Cosmochim. Acta 70, 1439–1456. https://doi.org/10.1016/j.gca.2005.11.014.

Gischler, E., Swart, P.K., Lomando, A.J., 2009. Stable isotopes of carbon and oxygen in modern sediments of carbonate platforms, barrier reefs, atolls and ramps: patterns and implications. In: Perspectives in Carbonate Geology. John Wiley & Sons, Ltd., pp. 61–74.

Grammer, G.M., Ginsburg, R.N., Swart, P.K., McNeill, D.F., Jull, A.J.T., Prezbindowski, D.R., 1993. Rapid growth rates of syndepositional marine aragonite cements in steep marginal slope deposits, Bahamas and Belize. J. Sediment. Res. 63, 983–989. https://doi.org/10.1306/D4267C62-2B26-11D7-8648000102C1865D.

Gussone, N., Ahm, A.-S.C., Lau, K.V., Bradbury, H.J., 2020. Calcium isotopes in deep time: potential and limitations. Chem. Geol. 544, 119601. https://doi.org/10.1016/j.chemgeo.2020.119601.

Hearty, P.J., 1998. The geology of Eleuthera Island, Bahamas: a Rosetta Stone of Quaternary stratigraphy and sea-level history. Quat. Sci. Rev. 17, 333–355. https://doi.org/10.1016/S0277-3791(98)00046-8.

Hearty, P.J., Tormey, B.R., Neumann, A., 2000. Discussion of "Palaeoclimatic significance of co-occurring wind- and water-induced sedimentary structures in the last-interglacial coastal deposits from Bermuda and the Bahamas" (Kindler and Strasser, 2000, Sedimentary Geology, 131, 1–7). Sediment. Geol. 147, 429–435. https://doi.org/10.1016/S0037-0738(01)00142-7.

Henderson, G.M., Lindsay, F.N., Slowey, N.C., 1999. Variation in bioturbation with water depth on marine slopes: a study on the Little Bahamas Bank. Mar. Geol. 160, 105–118. https://doi.org/10.1016/S0025-3227(99)00018-3.

Hermoso, M., 2016. Isotopic record of Pleistocene glacial/interglacial cycles in pelagic carbonates: revisiting historical data from the Caribbean Sea. Quat. Sci. Rev. 137, 69–78. https://doi.org/10.1016/j.quascirev.2016.02.003.

Higgins, J., Blättler, C., Lundstrom, E., Santiago-Ramos, D., Akhtar, A., Crüger Ahm, A.-S., Bialik, O., Holmden, C., Bradbury, H., Murray, S., Swart, P., 2018. Mineralogy, early marine diagenesis, and the chemistry of shallow-water carbonate sediments. Geochim. Cosmochim. Acta 220, 512–534. https://doi.org/10.1016/j.gca.2017.09.046.

Hodgin, E.B., Swanson-Hysell, N.L., DeGraff, J.M., Kylander-Clark, A.R., Schmitz, M.D., Turner, A.C., Zhang, Y., Stolper, D.A., 2022. Final inversion of the Midcontinent Rift during the Rigolet Phase of the Grenvillian Orogeny. Geology 50, 547–551. https://doi.org/10.1130/G49439.1.

Hoffman, J.S., Clark, P.U., Parnell, A.C., He, F., 2017. Regional and global sea-surface temperatures during the last interglaciation. Science 355, 276–279. https://doi.org/10.1126/science.aai8464.

Ingalls, M., Frantz, C.M., Snell, K.E., Trower, E.J., 2020. Carbonate facies-specific stable isotope data record climate, hydrology, and microbial communities in Great Salt Lake, UT. Geobiology 18, 566–593. https://doi.org/10.1111/gbi.12386.

Kim, S.-T., O'Neil, J.R., Hillaire-Marcel, C., Mucci, A., 2007. Oxygen isotope fractionation between synthetic aragonite and water: influence of temperature and Mg^{2+} concentration. Geochim. Cosmochim. Acta 71, 4704–4715. https://doi.org/10.1016/j.gca.2007.04.019.

Kindler, P., Hearty, P.J., 1996. Carbonate petrography as an indicator of climate and sea-level changes: new data from Bahamian Quaternary units. Sedimentology 43, 381–399. https://doi.org/10.1046/j.1365-3091.1996.d01-11.x.

Kindler, P., Strasser, A., 2000. Palaeoclimatic significance of co-occurring wind- and water-induced sedimentary structures in the last-interglacial coastal deposits from Bermuda and the Bahamas. Sediment. Geol. 131, 1–7. https://doi.org/10.1016/S0037-0738(99)00123-2.

Kump, L.R., Arthur, M.A., 1999. Interpreting carbon-isotope excursions: carbonates and organic matter. Chem. Geol. 161, 181–198. https://doi.org/10.1016/S0009-2541(99)00086-8.

LeGrande, A.N., Schmidt, G.A., 2006. Global gridded data set of the oxygen isotopic composition in seawater. Geophys. Res. Lett. 33. https://doi.org/10.1029/2006GL026011.

Lorens, R.B., 1981. Sr, Cd, Mn and Co distribution coefficients in calcite as a function of calcite precipitation rate. Geochim. Cosmochim. Acta 45, 553–561. https://doi.org/10.1016/0016-7037(81)90188-5.

Lowenstam, H.A., Epstein, S., 1957. On the origin of sedimentary aragonite needles of the Great Bahama Bank. J. Geol. 65, 364–375. https://doi.org/10.1086/626439.

Ludvigson, G.A., Witzke, B.J., González, L.A., Carpenter, S.J., Schneider, C.L., Hasiuk, F., 2004. Late Ordovician (Turinian–Chatfieldian) carbon isotope excursions and their stratigraphic and paleoceanographic significance. Palaeogeogr. Palaeoclimatol. Palaeoecol. 210, 187–214. https://doi.org/10.1016/j.palaeo.2004.02.043.

Lynts, G.W., 1970. Conceptual model of the Bahamian Platform for the last 135 million years. Nature 225, 1226–1228. https://doi.org/10.1038/2251226a0.

Melchin, M.J., Holmden, C., 2006. Carbon isotope chemostratigraphy of the Llandovery in Arctic Canada: implications for global correlation and sea-level change. GFF 128, 173–180. https://doi.org/10.1080/11035890601282173.

Milliman, J.D., Freile, D., Steinen, R.P., Wilber, R.J., 1993. Great Bahama Bank aragonitic muds; mostly inorganically precipitated, mostly exported. J. Sediment. Res. 63, 589–595. https://doi.org/10.1306/D4267B81-2B26-11D7-8648000102C1865D.

Morse, J.W., Andersson, A.J., Mackenzie, F.T., 2006. Initial responses of carbonate-rich shelf sediments to rising atmospheric pCO_2 and "ocean acidification": role of high Mg-calcites. Geochim. Cosmochim. Acta 70, 5814–5830. https://doi.org/10.1016/j.gca.2006.08.017.

Mullins, H.T., Lynts, G.W., 1977. Origin of the northwestern Bahama Platform: review and reinterpretation. Geol. Soc. Am. Bull. 88, 1447–1461. https://doi.org/10.1130/0016-7606(1977)88<1447:OOTNBP>2.0.CO;2.

Opdyke, B.N., Walker, J.C.G., 1992. Return of the coral reef hypothesis: basin to shelf partitioning of $CaCO_3$ and its effect on atmospheric CO_2. Geology 20, 733–736. https://doi.org/10.1130/0091-7613(1992)020<0733:ROTCRH>2.3.CO;2.

Patterson, W.P., Walter, L.M., 1994. Depletion of $\delta^{13}C$ in seawater ΣCO_2 on modern carbonate platforms: significance for the carbonate isotopic record of carbonates. Geology 22, 885–888. https://doi.org/10.1130/0091-7613(1994)022<0885:DOCISC>2.3.CO;2.

Pittet, B., Strasser, A., Mattioli, E., 2000. Depositional sequences in deep-shelf environments: a response to sea-level changes and shallow-platform carbonate productivity (Oxfordian, Germany and Spain). J. Sediment. Res. 70, 392–407. https://doi.org/10.1306/2DC40918-0E47-11D7-8643000102C1865D.

Pujalte, V., Baceta, J.I., Orue-Etxebarria, X., Payros, A., 1998. Paleocene strata of the Basque country, western Pyrenees, northern Spain: facies and sequence develepment in a deep-water starved basin. In: Mesozoic and Cenozoic Sequence Stratigraphy of European Basins, SEPM Special Publication, vol. 60. https://doi.org/10.2110/pec.98.02.0311.

Purkis, S., Cavalcante, G., Rohtla, L., Oehlert, A.M., Harris, P.M., Swart, P.K., 2017. Hydrodynamic control of whitings on Great Bahama Bank. Geology 45, 939–942. https://doi.org/10.1130/G39369.1.

Purkis, S.J., Harris, P.M., 2016. The extent and patterns of sediment filling of accommodation space on Great Bahama Bank. J. Sediment. Res. 86, 294–310. https://doi.org/10.2110/jsr.2016.24.

Purkis, S.J., Oehlert, A.M., Dobbelaere, T., Hanert, E., Harris, P.M., 2023. Always a White Christmas in the Bahamas: temperature and hydrodynamics localize winter mud production on Great Bahama Bank. J. Sediment. Res. 93, 145–160. https://doi.org/10.2110/jsr.2022.066.

Ridgwell, A., 2005. A Mid Mesozoic Revolution in the regulation of ocean chemistry. Mar. Geol. 217, 339–357. https://doi.org/10.1016/j.margeo.2004.10.036.

Schlager, W., Reijmer, J.J., Droxler, A., 1994. Highstand shedding of carbonate platforms. J. Sediment. Res. 64, 270–281. https://doi.org/10.1306/D4267FAA-2B26-11D7-8648000102C1865D.

Schobben, M., van de Velde, S., Gliwa, J., Leda, L., Korn, D., Struck, U., Ullmann, C.V., Hairapetian, V., Ghaderi, A., Korte, C., Newton, R.J., Poulton, S.W., Wignall, P.B., 2017. Latest Permian carbonate carbon isotope variability traces heterogeneous organic carbon accumulation and authigenic carbonate formation. Clim. Past 13, 1635–1659. https://doi.org/10.5194/cp-13-1635-2017.

Schoene, B., Eddy, M.P., Samperton, K.M., Keller, C.B., Keller, G., Adatte, T., Khadri, S.F., 2019. U-Pb constraints on pulsed eruption of the Deccan Traps across the end-Cretaceous mass extinction. Science 363, 862–866. https://doi.org/10.1126/science.aau2422.

Scussolini, P., Bakker, P., Guo, C., Stepanek, C., Zhang, Q., Braconnot, P., Cao, J., Guarino, M.-V., Coumou, D., Prange, M., Ward, P.J., Renssen, H., Kageyama, M., Otto-Bliesner, B., Aerts, J.C.J.H., 2019. Agreement between reconstructed and modeled boreal precipitation of the Last Interglacial. Sci. Adv. 5, eaax7047. https://doi.org/10.1126/sciadv.aax7047.

Solan, M., Ward, E.R., White, E.L., Hibberd, E.E., Cassidy, C., Schuster, J.M., Hale, R., Godbold, J.A., 2019. Worldwide measurements of bioturbation intensity, ventilation rate, and the mixing depth of marine sediments. Sci. Data 6, 58. https://doi.org/10.1038/s41597-019-0069-7.

Staudigel, P.T., Swart, P.K., 2019. A diagenetic origin for isotopic variability of sediments deposited on the margin of Great Bahama Bank, insights from clumped isotopes. Geochim. Cosmochim. Acta 258, 97–119. https://doi.org/10.1016/j.gca.2019.05.002.

Swart, P.K., 2008. Global synchronous changes in the carbon isotopic composition of carbonate sediments unrelated to changes in the global carbon cycle. Proc. Natl. Acad. Sci. 105, 13741–13745. https://doi.org/10.1073/pnas.0802841105.

Swart, P.K., Eberli, G., 2005. The nature of the $\delta^{13}C$ of periplatform sediments: implications for stratigraphy and the global carbon cycle. Sediment. Geol. 175, 115–129. https://doi.org/10.1016/j.sedgeo.2004.12.029.

Swart, P.K., Oehlert, A., Mackenzie, G., Eberli, G.P., Reijmer, J., 2014. The fertilization of the Bahamas by Saharan dust: a trigger for carbonate precipitation? Geology 42, 671–674. https://doi.org/10.1130/G35744.1.

Swart, P.K., Reijmer, J.J., Otto, R., 2009. A re-evaluation of facies on Great Bahama Bank II: variations in the $\delta^{13}C$, $\delta^{18}O$ and mineralogy of surface sediments. In: Perspectives in Carbonate Geology. John Wiley & Sons, Ltd., pp. 47–59. https://onlinelibrary.wiley.com/doi/abs/10.1002/9781444312065.ch4.

Vimpere, L., Del Piero, N., Shawwa, N.A., Beguelin, K., Kindler, P., Castelltort, S., 2021. Upper Pleistocene parabolic ridges (i.e. 'chevrons') from the Bahamas: storm-wave sediments or aeolian deposits? A quantitative approach. Sedimentology 68, 1255–1288. https://doi.org/10.1111/sed.12828.

Watkins, J.M., Hunt, J.D., Ryerson, F.J., DePaolo, D.J., 2014. The influence of temperature, pH, and growth rate on the $\delta^{18}O$ composition of inorganically precipitated calcite. Earth Planet. Sci. Lett. 404, 332–343. https://doi.org/10.1016/j.epsl.2014.07.036. https://www.sciencedirect.com/science/article/pii/S0012821X14004919.